Evolution of intermittent filaments in the scrape-off layer of NSTX

M. Lampert,[1] A. Diallo,[1] and J. R. Myra[2]
[1)]*Princeton Plasma Physics Laboratory, Princeton, NJ, United States of America*[a)]
[2)]*Lodestar Research Corporation, Broomfield, CO, United States of America*

Filamentary structures naturally arise from background turbulence in the scrape-off layer (SOL) of plasmas, leading to significant particle and heat transport that can degrade overall plasma confinement. This enhanced transport can contribute to unacceptably high heat loads on plasma-facing components. As such, understanding the physics of SOL plasma filaments is critical for predicting and mitigating their effects in future fusion devices.

On the National Spherical Torus Experiment (NSTX), plasma filaments—commonly referred to as "blobs"—were investigated using the gas-puff imaging (GPI) diagnostic in the edge and SOL regions. The analysis involved identifying, segmenting, and tracking the characteristic contours of the blobs in each frame of GPI video sequences. Their evolution was characterized through shape descriptors, velocity, and angular velocity derived from their contour coordinates.

The results indicate that as the blob area increases, their shapes become more concave and less circular, suggesting reduced structural stability in larger blobs. This result aligns with previous theoretical results where it was shown that larger blobs are more susceptible to instabilities[1,2]. A positive correlation was observed between radial velocity and radial position, suggesting radially outward acceleration of the filaments, potentially driven by decreasing viscous drag towards the far SOL. Interestingly, blobs in background SOL turbulence exhibited minimal spinning in contrast to filaments originating from ELMs, which show substantial rotation during their paths[3]. Statistical analysis of the solidity and total curvature shape descriptors, along with their temporal evolution, revealed relatively broad, near-Gaussian distributions. This suggests that blob morphology is strongly influenced by stochastic turbulent processes in the surrounding plasma environment.

Blob parameters were also compared with bulk plasma and radial profile measurements. Notable trends were found between blob rotation and poloidal velocity with collisionality and line-integrated density. These findings contribute to a deeper understanding of blob dynamics and provide valuable insights for refining SOL turbulence models.

I. INTRODUCTION

Turbulence in the scrape-off layer (SOL) of tokamak plasmas results in substantial heat and particle losses from the confined core plasma. This turbulence is predominantly intermittent and manifests as discrete filamentary structures with elevated density and temperature compared to the background plasma. These filaments are aligned along the magnetic field lines, with poloidal cross-sections resembling blobs, hence the commonly used term blob-filaments, or blobs. Blobs play a significant role in radial particle transport, contributing to confinement degradation and increased heat flux to plasma-facing components. Such structures have been observed across a wide range of magnetic confinement devices, including tokamaks (e.g., DIII-D[4], NSTX[5]), stellarators[6], and linear plasma devices[7], as well.

Previous research has primarily focused on aspects such as the relative blob fraction[8], blob generation rates[9], formation mechanisms[10], and basic blob characteristics including velocity and size[11]. The temporal and spatial structures of blobs have been explored in studies by Zweben[11,12]. However, detailed investigation into the morphological evolution of blobs has been limited. Prior work has largely concentrated on changes in blob elongation due to interactions with the edge shear layer[9], without extending to more comprehensive shape descriptors such as convexity, roundness, solidity, or total curvature.

Visual inspection of gas-puff imaging (GPI) videos on the NSTX (National Spherical Torus Experiment) tokamak exhibited interesting morphology evolution of filamentary structures. A more complex morphological evolution was seen than the typically investigated structure elongation and tilting. The conventional analysis techniques typically utilize two-dimensional Gaussian or ellipse fits, which are insufficient to capture fine details or temporal changes in blob morphology. Understanding the evolution of blob shape could provide deeper insights into the driving physics mechanisms behind blob evolution and their contribution to radial transport.

The structure of the paper is as follows. Section II provides an overview of the experimental setup, including the NSTX tokamak and the gas-puff imaging (GPI) diagnostic. Section III outlines the analysis methodology, detailing the pre-processing steps, blob structure identification, segmentation and tracking procedures, as well as the shape descriptors used. Section IV presents the results, including both a detailed analysis of a single discharge and a statistical evaluation of the complete blob database. The results are discussed in Section V. Finally, Section VI summarizes the key findings of the study.

II. EXPERIMENTAL SETUP

The results presented in this paper are based on measurements obtained using the gas-puff imaging (GPI) diagnostic[13] on the National Spherical Torus Experiment (NSTX) tokamak[14]. A brief overview of these systems is provided below, while detailed descriptions can be found in their

[a)]The author to whom correspondence may be addressed: mlampert@pppl.gov

respective references.

A. The NSTX tokamak

NSTX is a medium-sized, low-aspect-ratio spherical tokamak located in Princeton, NJ, USA. It has a major radius of $R = 0.85$ m and a minor radius of $a = 0.67$ m, resulting in an aspect ratio of $R/a \geq 1.26$. The maximum toroidal field achievable is $B_T = 0.6$ T. Plasma heating is provided by up to 5 MW of neutral beam injection (NBI) and 6 MW of high-harmonic fast wave (HHFW) heating.

B. Gas-puff imaging (GPI)

Gas-puff imaging utilizes a puff of neutral gas in the SOL and edge plasma to enhance the local light emission. Gas neutrals get excited through collisional excitation with the plasma electrons and emit light during de-excitation. As filamentary structures in the SOL and edge plasma pass through the gas-cloud region, they excite the gas neutrals. The emitted light is a function of the local electron density and temperature, and can be used to investigate their sizes, velocities, and shapes.

Figure 1 illustrates the gas-puff imaging (GPI) setup on the NSTX tokamak. Deuterium gas is introduced through a gas manifold (indicated in pink), forming a quasi-two-dimensional gas cloud (red) that is observed through a viewport (green) along a viewing direction (cyan) nearly parallel to the magnetic field lines (yellow). A hypothetical plasma filament is depicted in orange. The radial (r) and poloidal (z) bi-normal directions are indicated in white.

The gas cloud is imaged using a fast visible camera (Vision Research Phantom v710) through a D_α band-pass interference filter. The temporal resolution is 2.5 μs with an exposure time of 2.1 μs. The pixel resolution is 64×80 (radial $\times$ poloidal) with each pixel covering an area of 3.75 mm $\times$ 3.75 mm. The camera has a dynamic range of 12 bits, and the exposure time was selected to prevent saturation. The effective optical resolution is approximately 10 mm. During the experiments, Deuterium was injected for approximately 50 ms.

The GPI diagnostic on NSTX does not allow for independent resolution of local plasma parameters, such as electron density and temperature, due to the nonlinear dependence of the emitted light intensity on both quantities. Nonetheless, the measured emission provides valuable spatial and temporal information about filamentary structures. When combined with independently measured or inferred plasma parameters from complementary diagnostics, GPI data can be effectively used to investigate correlations between blob position, velocity, and morphology. This enables further insight into the underlying physical mechanisms governing blob evolution.

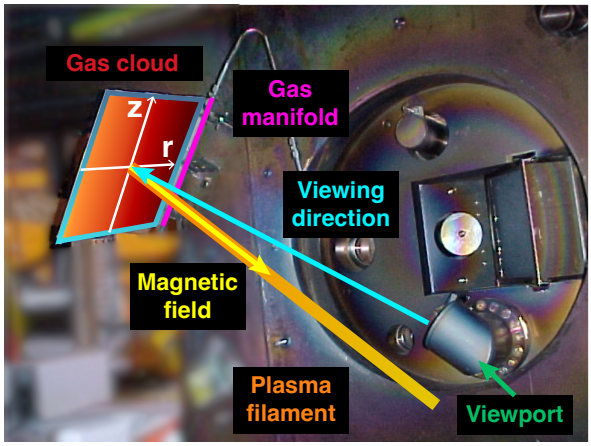

FIG. 1. The gas-puff imaging setup on NSTX illustrating the approximate magnetic field direction (yellow), viewing direction (cyan), gas manifold (pink), and gas cloud location (red). A hypothetical plasma filament is shown in orange.

Parameter	Range	
Toroidal field	B_T	$0.33 - 0.54$ T
Plasma current	I_p	$0.6 - 1.2$ MA
Electron density	$< n_e >$	$1.3 - 6.2 \cdot 10^{20}$ m^{-3}
Greenwald-fraction	n_e/n_{GW}	$0.19 - 0.96$
Heating	P_{aux}	$0 - 6$ MW

TABLE I. Plasma parameter ranges for the discharges in the blob database: toroidal magnetic field (B_T), plasma current (I_p), line averaged electron density ($< n_e >$), and total auxiliary heating power (P_{sum}).

C. Blob database

To characterize the blob evolution in NSTX plasmas, a database was constructed using data from 86 plasma shots in which the GPI diagnostic was available. Only shots without edge localized mode (ELM) bursts near the time of peak GPI signal were included. The shots included low confinement L-mode and high confinement H-mode shots in both NBI and HHFW heating scenarios. Although GPI was measuring for 200 ms from the time of the gas injection, the analysis was limited to a ± 5 ms window around the peak light emission where the signal-to-noise ratio was the highest. In cases where large transient events, such as edge localized modes (ELMs), occurred within this window, the interval was adjusted to exclude the transient peak. Key plasma parameters of the discharges included in the database are summarized in Table I.

As previously noted, the database includes both L-mode and H-mode discharges. Significant differences in blob dynamics are not expected between these confinement regimes[15]. While the blob generation rate and waiting time distribution may vary due to the suppression of edge turbulence in H-mode plasmas, detailed investigation of these aspects was beyond the scope of this study. Nevertheless, separate results of the analyses for L- and H-mode discharges can be found under the supplementary material in the Data Stor-

age under Ref. 16 for the curious reader. Detailed discussion of these results is not provided there, it is reserved for a future publication.

III. METHODOLOGY

This section presents the methods used to process GPI data, including blob identification, segmentation, tracking, and shape descriptor estimation. While each of these techniques has been applied individually in previous studies - such as the pre-processing steps in ELM filament analysis[3,17], structure identification in fast camera data[18], object tracking in traffic analysis[19], and shape characterization[20] — their combined application in the context of fusion plasma research is unprecedented. The complete suite of data analysis tools developed for this work is openly available in the corresponding GitHub repository under Ref. 21.

Multiple blob-tracking algorithms have been developed for analyzing GPI data across different fusion devices. Prior methods implemented on Alcator C-Mod[22], NSTX[11], and TCV (Tokamak à configuration variable)[23] typically relied on identifying contours exceeding a fixed intensity threshold, with tracking performed using binary overlap, non-overlap criteria. On MAST-U, a watershed-based segmentation approach was applied to fast-camera imaging data[18]; however, filament tracking was not pursued.

The method presented in this study offers advantages over these approaches by incorporating enhanced watershed segmentation capable of resolving closely spaced and even touching structures. Furthermore, tracking is performed using the intersection-over-union (IoU) metric, which provides a robust framework for handling filament merging and splitting events, and it can resolve tracking of multiple adjacent structures more efficiently than the binary overlap-based tracking schemes. These aspects of our watershed-based filament identification and tracking method represent key advantages of the methodology over traditional contour-based tracking algorithms.

A. Pre-processing

The pre-processing steps used in this analysis follow the procedures described in detail in Ref.[17]; therefore, only a brief summary is provided here.

In gas-puff imaging data analysis, the emission from neutral gas atoms responding to the slowly varying plasma background must be suppressed to isolate light emission originating from the intermittent fluctuations. This is achieved by applying an elliptic infinite impulse response filter with a 1 kHz bandwidth. To mitigate edge effects and filter-induced oscillations at the temporal boundaries, the data is symmetrically extended by $\pm$1ms before filtering.

In GPI diagnostic measurements, the signal can be approximately modeled as the product of the fluctuating plasma density, the spatial distribution of neutral gas atoms in the background and the electron density distribution of the background plasma. The latter two terms vary slowly in time and can be approximated by the low-frequency component of the light emission measured by the GPI diagnostic. To suppress this background contribution, the original GPI signal is divided by the filtered signal. This normalization approach was found to be more effective than background subtraction in isolating the fluctuating component of interest.

As a final pre-processing step, a threshold is applied to the normalized data: at each time point, pixels with values below the threshold are set to zero. The threshold level is defined as the mean signal plus one standard deviation over the selected time interval.

B. Filament identification

Before characterizing the evolution of SOL filaments, they must first be identified and segmented within the GPI video frames. This is achieved using the watershed segmentation technique[24], which is well-suited for separating distinct, overlapping, or adjacent structures.

The traditional watershed method begins by identifying object contours and computing the distance transform[25], which assigns each pixel a value based on its distance from the nearest background pixel. The peaks in the distance-transformed image are treated as local minima in an inverted topographical surface — analogous to the lowest points in a landscape — where virtual "water sources" are placed. Water is then allowed to fill these basins until it reaches either a predefined threshold or encounters another growing region. In the latter case, a boundary or "watershed" is constructed between the competing regions, effectively separating the objects. This makes the method particularly effective for identifying occluded or closely packed structures.

To adapt this technique for GPI image segmentation, several modifications were implemented, as described in the following paragraphs.

To apply the watershed segmentation technique, the image must first be separated into object and background pixels. This is accomplished using Otsu's thresholding method[26], which analyzes the histogram of pixel intensities to identify two dominant peaks corresponding to object and background regions. The optimal threshold is chosen to minimize intra-class variance between these two groups. This method is effective when the objects are distinguishable from the background and exhibit relatively uniform intensity. These conditions are satisfied in GPI measurements.

Blobs in scrape-off layer plasmas can be reasonably approximated as two-dimensional Gaussian-like structures, which resemble the distance-transformed shapes of regular objects typically analyzed using watershed segmentation (see, for example, Fig. 4 in Ref. 25). Consequently, the distance transform step is omitted in the present workflow. Instead, source locations for the watershed algorithm are directly assigned to the intensity maxima within the perimeters of the preliminarily segmented structures. To prevent over-segmentation, a minimum separation of 5 pixels is enforced

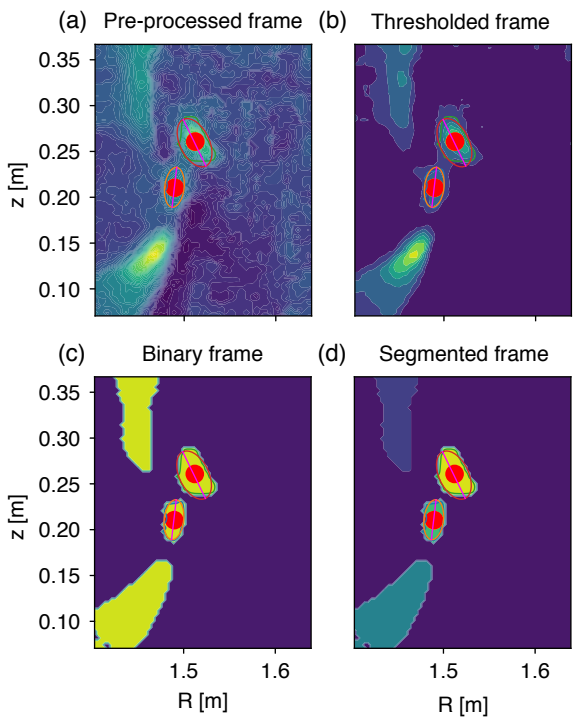

FIG. 2. Steps of the watershed segmentation process: (a) raw GPI frame; (b) pre-processed frame after background suppression; (c) binary frame showing separation of structure and background; (d) final segmented structures, with different colors representing distinct structures.

between source points. Following this, the segmented structures are labeled, and their characteristic contour polygons are computed. The steps of the watershed segmentation are depicted in Fig. 2.

These segmentation steps are applied to each frame of the GPI video sequence. The resulting data are compiled into a database that records the contour polygon of each identified structure in every frame. At this stage, however, no temporal correspondence is established between structures in consecutive frames — that is, the structures are not yet tracked over time.

C. Structure tracking

Once structures are identified and segmented in individual frames, they must be tracked to establish temporal continuity, i.e., assign consistent labels to the same structure as it evolves from the time of its appearance until its disappearance.

In earlier NSTX GPI studies[5,17], tracking was primarily performed by evaluating the intersection of contour polygons between consecutive frames. However, this approach is prone to errors in cases where multiple structures are in close proximity or overlapping, leading to ambiguous matches.

To address this limitation, the intersection-over-union (IoU)

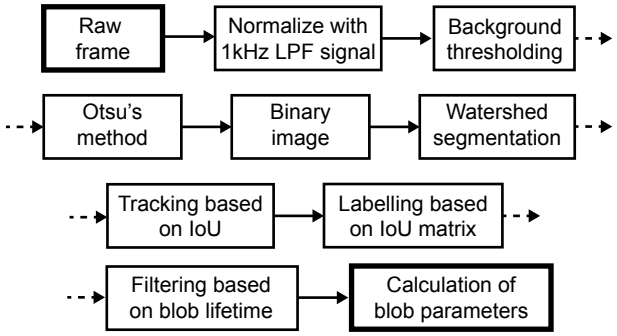

FIG. 3. Flowchart illustrating the watershed-based identification and segmentation process, followed by the Intersection-over-Union (IoU) metric–based tracking method.

metric is employed[19]. IoU is a dimensionless quantity defined as the ratio of the area of intersection to the area of union between two structures in consecutive frames. This metric is computed for all overlapping structure pairs across adjacent frames and compiled into a score matrix. While additional metrics, such as the pairwise correlation coefficient or normalized differences of shape descriptors, can be incorporated into the score matrix, they were found to introduce noise or ambiguity. As a result, the IoU metric alone was selected for optimal tracking performance.

To establish temporal correspondences between structures, the score matrix must be converted into a tracking matrix. This is commonly achieved using the Hungarian algorithm[27], which solves the assignment problem by optimizing the overall matching cost. However, in the present analysis, this method was found to yield suboptimal results, particularly in the context of close-proximity or overlapping filamentary structures. Instead, a simpler maximum-score selection approach was adopted, which provided more reliable tracking outcomes.

In this method, for each row of the score matrix, the entry with the highest IoU score is set to "1" in the tracking matrix, while all other entries are set to "0". Unique numerical labels are then assigned to structures based on these maximum-score associations, allowing consistent identification of each blob throughout its observation. A flowchart summarizing the tracking procedure is shown in Fig. 3.

D. Shape descriptors

Shape descriptors provide quantitative metrics to characterize the geometry of structures. Effective shape descriptors are invariant to size, translation, and rotation, enabling consistent comparison across varying conditions. Different descriptors capture distinct aspects of shape and its evolution. A comprehensive discussion of these metrics can be found in Ref. 20. Here, a list of key shape descriptors is provided along with a brief description.

- Convex hull: The smallest convex polygon that fully encloses the structure, used as a reference for several derived metrics.
- Convexity: Defined as the ratio of the perimeter of the convex hull to the perimeter of the actual structure.
- Roundness: Calculated as the ratio of the structure's area to the square of its convex hull perimeter, normalized such that a perfect circle yields a roundness of one.
- Solidity: The ratio of the structure's area to the area of its convex hull.
- Total curvature: The average curvature computed across all vertices of the polygon, based on the angles formed by neighboring vertex triplets along the perimeter.

These shape descriptors are computed for the characteristic contour polygons of each identified and tracked blob for each time point of their observation across all shots in the blob database.

Shape descriptors may be influenced by measurement noise if the signal-to-noise ratio (SNR) is insufficient. These descriptors are derived from the contours of the identified structures, which are determined based on the measured light intensity. At low light levels, this intensity is inherently noisy due to photon statistics. However, in GPI diagnostic measurements analyzed in this study—focused around the peak emission levels—the SNR typically ranges between 100 and 200. At these levels, significant distortion of the structure shapes due to noise is not expected.

The dynamic range of the camera can also influence the accuracy of the results, particularly if the light intensity is poorly resolved or if saturation occurs. In this study, a 12-bit camera was used, providing sufficient resolution to accurately capture the intensity variations necessary for analyzing blob filament shapes. Additionally, the camera exposure time was chosen to avoid saturation while maintaining the peak detected intensity close to the maximum allowable range for optimal dynamic range.

E. Additional estimated parameters

In addition to shape descriptors, further blob parameters were derived from the characterizing polygon and the fitted ellipse. The area of each blob was calculated using the surveyor's (or shoelace) formula applied to the polygon's vertex coordinates[28]. Similarly, the polygon's perimeter was computed from these coordinates and was subsequently used in the evaluation of several shape descriptors.

Each identified structure was characterized by fitting an ellipse to its polygonal boundary. The fitted ellipse provided key geometric parameters, including the lengths of the semi-major and semi-minor axes, the centroid, and the orientation angle of the major axis relative to the horizontal. The angular velocity of the structures was determined from the temporal derivative of this orientation angle. Elongation was computed based on the projected lengths of the ellipse axes onto the radial and poloidal directions.

The position of each structure can be estimated using multiple methods. One approach calculates the centroid by averaging the coordinates of the polygon's vertices. Alternatively, the center of the fitted ellipse can be used. A third method applies the center-of-gravity (COG) formula, averaging the pixel coordinates within the polygon weighted by pixel intensity (analogous to mass in the COG formula). All three position estimates were computed for each structure, and the resulting trends and correlations were found to be nearly identical. For consistency, the fitted ellipse center is used to define position throughout this paper. The velocity of the structures is derived from the temporal derivative of this position.

IV. RESULTS

A. Evolution of blob shape in an H-mode plasma

The structure identification algorithm was initially applied to a single GPI measurement from an H-mode plasma discharge, #141319. An example sequence of identified structures is shown in Fig. 4. Structures intersecting the edges of the measurement frame were excluded from the analysis to avoid boundary artifacts. The figure demonstrates that multiple blobs propagate within the observation region and undergo shape evolution as they propagate radially outward and poloidally downward, consistent with motion in the ion diamagnetic drift direction.

The results of the shape descriptor analysis for the example shot (#141319) are presented in Fig. 5. To illustrate the tracking performance of the algorithm, the radial and poloidal positions of the tracked blobs are also included. A selected subset of shape descriptors is shown, namely: area, orientation angle, roundness, and total curvature. To eliminate structures arising from noise or insufficient tracking, only those observed for a minimum duration of 25 μs (equivalent to 10 frames) were included in the analysis.

Figures 5(a) and (b) display the temporal evolution of the radial and poloidal positions, respectively. These plots demonstrate that, for most structures, the tracking algorithm achieves smooth and consistent blob tracking. Notably, the algorithm successfully tracks multiple structures simultaneously, as observed around t = 0.5440 s and t = 0.5467 s.

Figure 5(c) shows the evolution of blob area over time. Most tracked structures exhibit areas in the range of approximately 50 - 200 mm^2. No clear trend is observed in the depicted time range.

Figure 5(d) presents the evolution of the angle of the blob's major semi-axis obtained from ellipse fitting. No clear characteristic trend of the orientation is seen in this result.

Figure 5(e) presents the temporal evolution of the blob's roundness. In some cases, an increase in roundness is observed at the onset of the blob's trajectory, followed by a decrease towards the end of the observation period. However, the opposite behavior is also visible in certain instances,

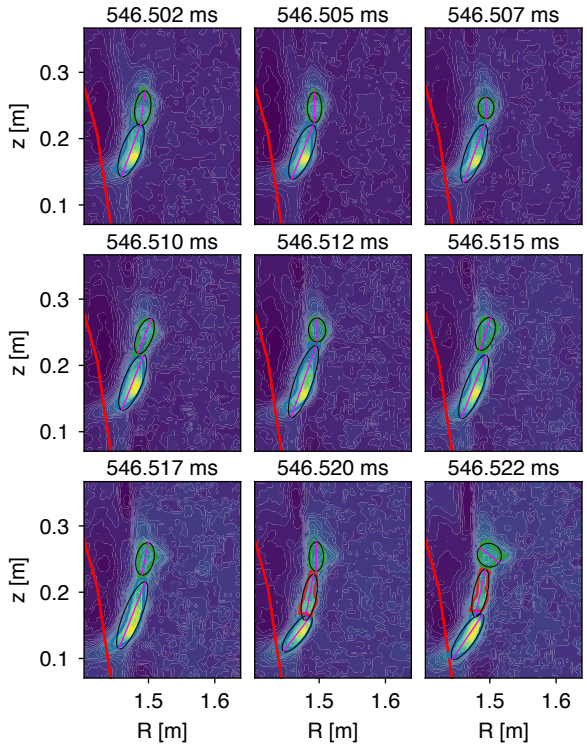

FIG. 4. Example of identified and tracked blobs in shot #141319. For each structure, the characteristic contour (different colors), the corresponding fitted ellipse (black), and the major semi-axis (magenta) are shown. Different colors indicate distinct tracked blobs. Structures that intersect the edges of the observation frame are excluded from the analysis. These tracked blobs were not filtered for their observation time. The red curve in each sub-plot represents the separatrix calculated by the automatic equilibrium reconstruction tool, EFIT (Equilibrium Fitting), for the discharge.

for example, at t = 0.5477 s, indicating that the evolution of roundness is not uniform across all tracked structures. As shown in Fig. 5(f), no systematic or consistent trend is observed in the total curvature throughout the displayed time interval either.

While the preliminary assessment of GPI video sequences revealed notable blob shape evolution, the analysis of a single time series does not provide conclusive evidence of characteristic behavior. To gain a more comprehensive understanding, a statistical evaluation of the shape descriptors across the entire database is necessary. This broader analysis is presented in Section IV B.

B. Statistical analysis of filament parameters

Following the inconclusive findings from the single H-mode shot analyzed in Section IV A, a statistical analysis was conducted on the full blob database. After filtering out discharges containing edge-localized modes (ELMs) around the peak intensity of GPI measurements, 86 shots remained in the dataset. In total, 11075 blobs were identified, segmented, and tracked, each persisting in the field of view for a minimum duration of 25 μs.

1. *Filament parameter histograms*

As a first step, the distributions of shape descriptors and filament parameters are analyzed. Figure 6 presents histograms of these parameters (previously shown in Fig. 5) along with their corresponding numerical time derivatives. In Fig. 6, filament parameters are evaluated on a frame-by-frame basis for each identified blob, without any temporal averaging. Consequently, rapid variations in filament parameters between consecutive frames are preserved in the analysis rather than being smoothed out.

Fig. 6(a) and (b) show the histograms of the blob area and its temporal change, respectively. The area distribution is positively skewed, with a peak at approximately 12 cm^2. The distribution of the area change (i.e., numerical derivative of the area) is slightly negatively skewed, indicating that blobs tend to shrink over time. However, the skewness of -0.1 suggests that this shrinking trend is relatively weak.

Fig. 6(c) and (d) display the angle and angular velocity distributions. In this context, the angular velocity refers to the spinning of the blob about its own axis, defined as the temporal rate of change of its tilt angle. This is distinct from the term blob rotation, which typically denotes the combined poloidal and toroidal motion around the torus. The angle distribution peaks at 1.36 rad (approximately 78 degrees), indicating a preferential alignment close to the poloidal direction. The angular velocity is approximately normally distributed with a mean near 0 rad/s, implying no systematic spinning for blobs. The (tilt) angle of blobs was previously studied by Zweben et al in Ref.[11]. Fig. 6(f) therein depicts the tilt angle vs radius for Ohmic and H-mode plasmas. Significant rotation is not observed for Ohmic plasmas from $R = R_{sep} - 2$ cm to $R = R_{sep} + 6$ cm; however, spinning was found for H-mode blobs at the level of $\omega \approx 545 \mathrm{rad/s}$ (calculated from the approximate tilt of 10, 8 cm radial distance and 500 m/s radial velocity). This study, however, only considered 7 H-mode discharges with 820 identified blobs. Those relatively low statistics therein could have contributed to their different results; however, further investigation is needed to uncover this difference, that is outside the scope of this current paper.

Fig. 6(e) and (f) present the distribution of the roundness parameter and its temporal derivative. The distribution of roundness peaks at 0.82, although values as low as 0.25 are observed, indicating significant deviation from a circular shape (roundness equals 1 for a perfect circle). The derivative of the roundness is slightly positively skewed (skewness = 0.232) indicating that blobs tend to evolve into shapes with higher roundness. The distribution deviates from Gaussian, indicated by a kurtosis of 3.8 (compared to 1 for a Gaussian distribution).

Fig.6(g) and (h) show the distributions of the total curvature and its temporal derivative. The distribution of the total

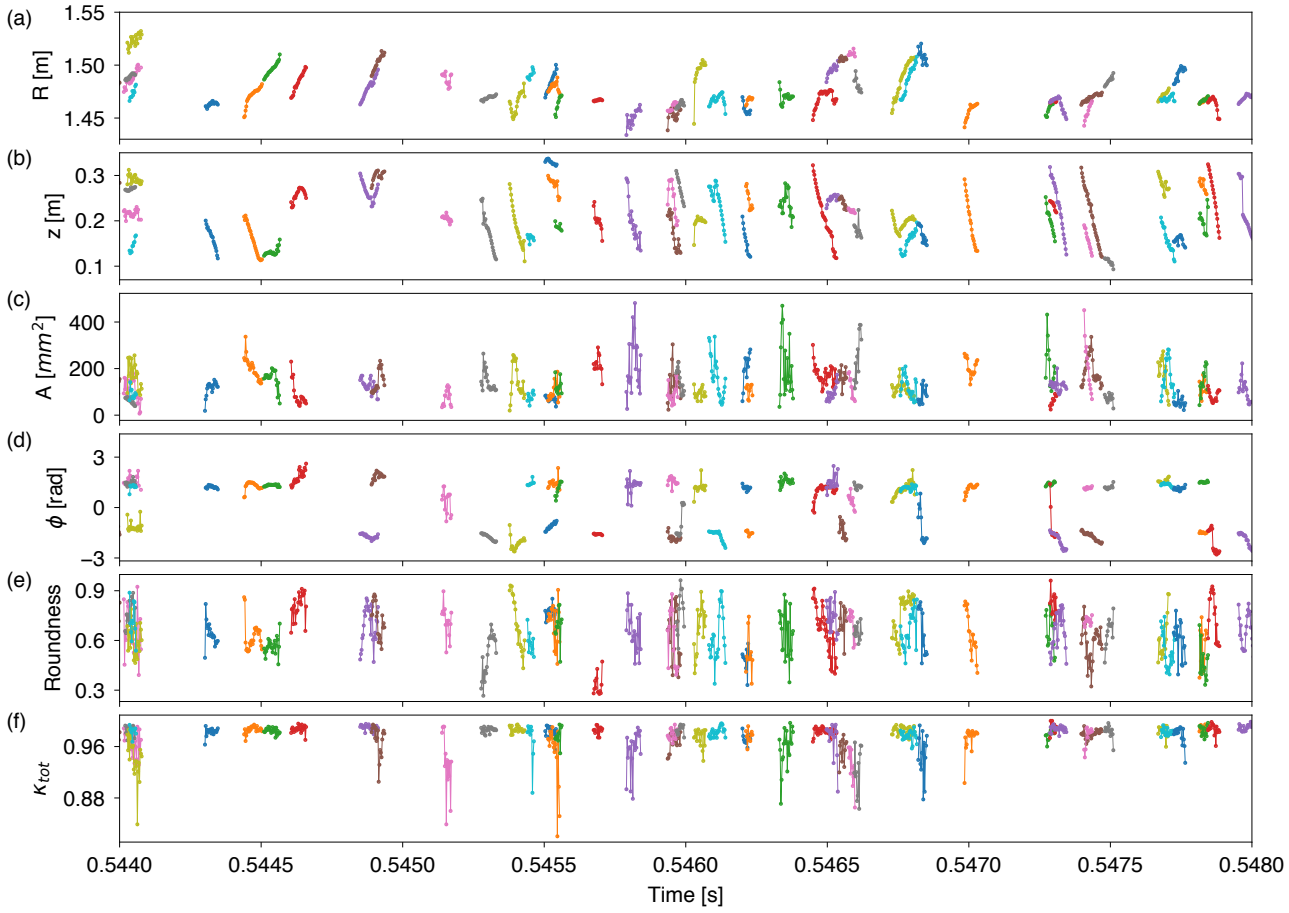

FIG. 5. Structure tracking and shape descriptor analysis for shot #141319. Shown are the temporal evolutions of the (a) radial position, (b) poloidal position, (c) area, (d) orientation angle of the fitted ellipse, (e) roundness, and (f) total curvature of the tracked blobs.

curvature is peaked at $\kappa = 0.98$. The curvature has an upper limit of one corresponding to the pixel size, suggesting that the characteristic contour of the identified structure is created from mostly right-angled corners. Consequently, this estimate is not reflective of the actual shape of the structures but is a result of the pixelated measurement. Smoothing the contours was attempted with fourth-order splines; however, the result introduced artifacts. Further analysis of the total curvature was outside the scope of this paper.

2. *Pearson matrix*

To investigate interdependencies among the estimated blob parameters, zero-lag Pearson correlation coefficients were computed for all parameter pairs. The calculations were performed without temporal averaging; instead, data arrays were constructed for each estimated parameter across all identified blobs and discharges, and correlations were evaluated directly on these datasets.

Correlations falling below a significance threshold were excluded from the matrix (white squares). This threshold was calculated by following these steps:

- Generating as many random number pairs as the number of data points that are correlated.
- Calculating the Pearson correlation coefficient between the random number pairs.
- Repeating these steps 10000 times and calculating the mean and variance of the correlation coefficients.
- Setting the threshold to the mean Pearson correlation coefficient plus two sigma.

Following these steps for the 11075 blobs and the resulting 221895 data points, the correlation threshold was set to 0.43%.

After calculating the pair-wise correlation coefficients, the result is stored in the so-called Pearson matrix. The matrix is comprising 11×11 key parameters, and is shown in Fig. 7.

Based on these results, eight notable and non-trivial parameter dependencies with relatively high correlation coefficients were identified. These parameter pairs are further analyzed in Section IV B 3.

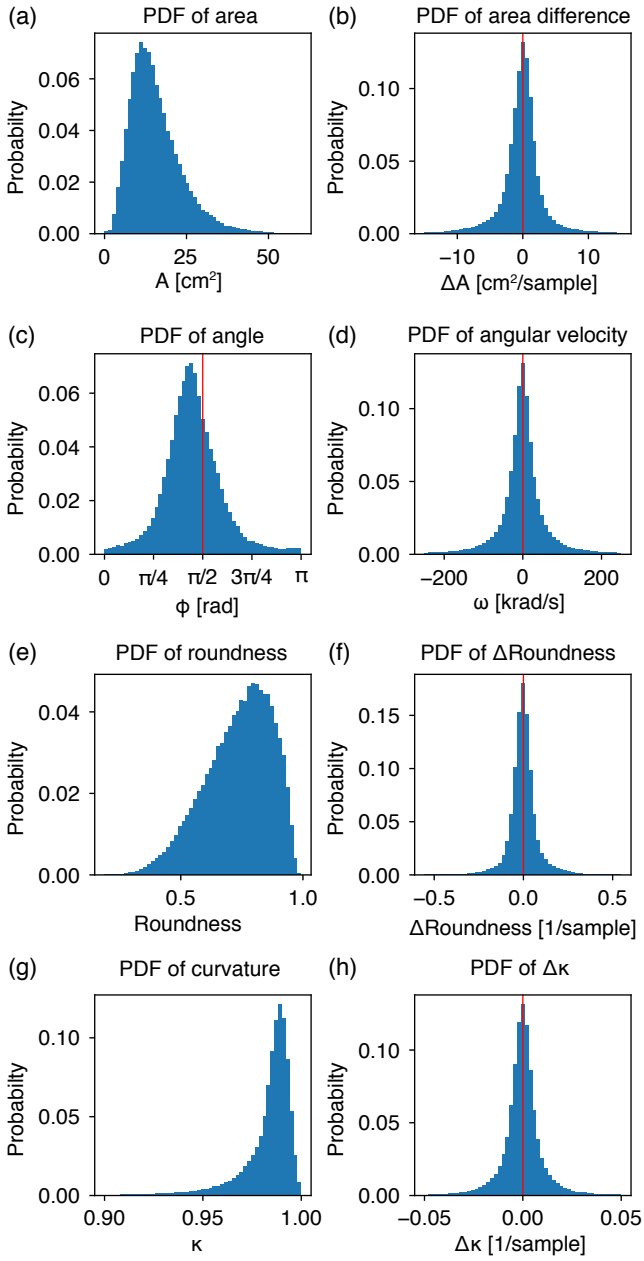

FIG. 6. Distributions of blob parameters and their time derivatives: (a), (b) area and its difference; (c), (d) angle and its time derivative; (e), (f) roundness and its time derivative; (g), (h) total curvature and its time derivative.

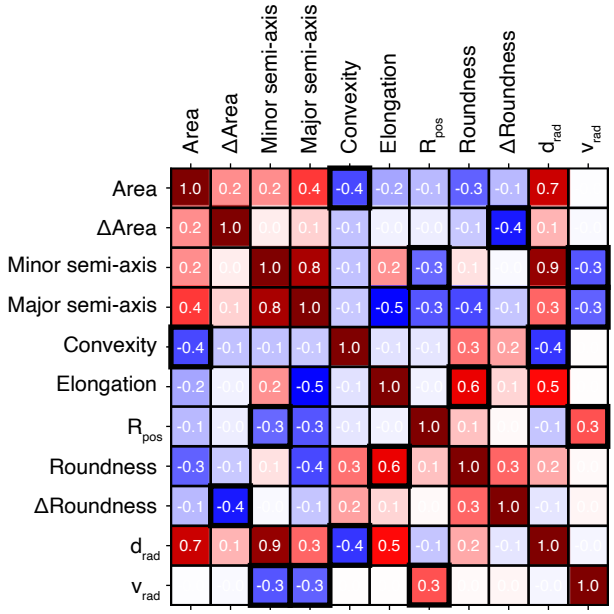

FIG. 7. Pearson matrix of the parameter correlations for the estimated blob parameters. (R_{pos} is the radial position, d_{rad} is the radial size, and v_{rad} is the radial velocity of the blobs.)

3. *Parameter dependence: two-dimensional distributions*

Following the calculation of the Pearson matrix, the pairwise dependencies between blob parameters were further examined by evaluating their two-dimensional probability distributions. The resulting distributions are presented in Figure 8.

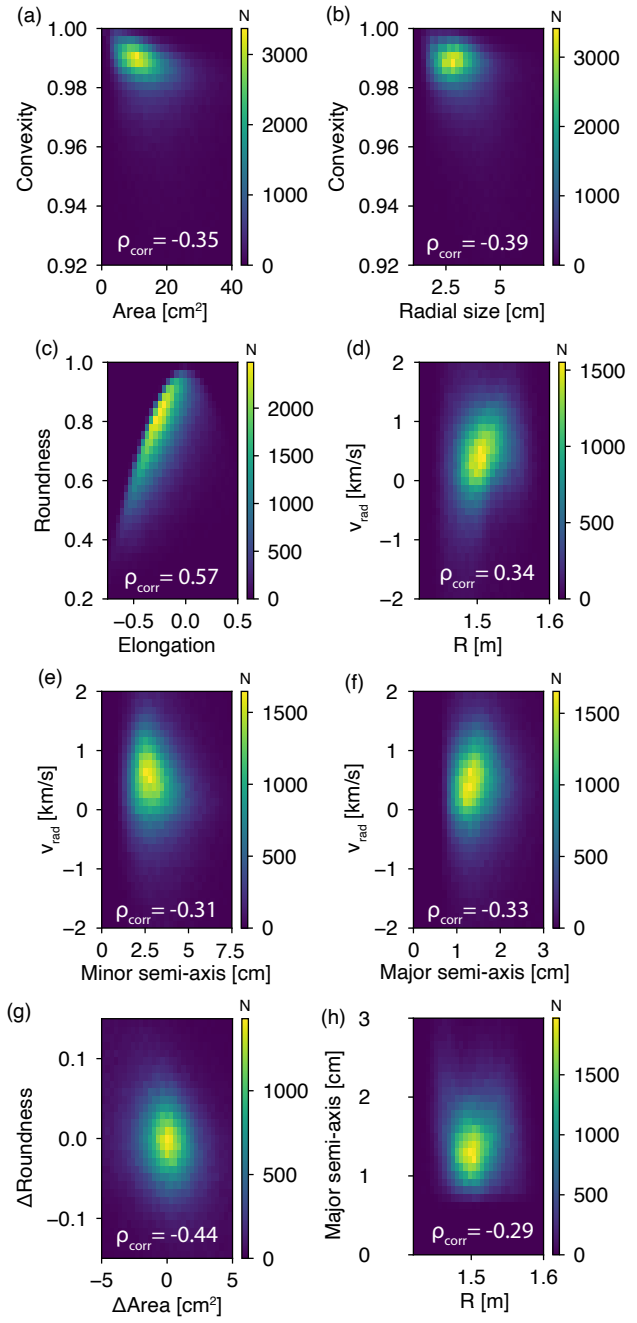

FIG. 8. Two-dimensional probability distributions of selected filament parameters, along with their Pearson correlation coefficients. (a) Area vs. convexity; (b) Radial size vs. convexity; (c) Elongation vs. roundness; (d) Radial position vs. radial velocity; (e) Major semi-axis vs. radial velocity; (f) Minor semi-axis vs. radial velocity; (g) Area ratio vs. roundness difference; (h) Radial position vs. major semi-axis.

Figure 8(a) shows the joint distribution of blob area and convexity. A significant negative correlation is observed, indicating that larger filaments tend to exhibit more concave shapes. One speculative explanation for this behavior is that larger blobs may be more susceptible to instabilities[1,2], which could result in increasingly concave morphologies and eventual breakup into smaller, more convex structures. A similar trend is evident in Fig. 8(b), where radial size is plotted against convexity. A strong negative correlation is found here, as well.

Figure 8(c) displays the correlation between elongation and roundness. A significant positive correlation is observed between these parameters. However, since elongation is predominantly negative and roundness is a positive-definite quantity, this result indicates that greater absolute elongation corresponds to a reduction in roundness. Although elongation is derived from the fitted ellipse parameters, and roundness is calculated directly from the polygonal contour, their relationship is likely driven by their shared geometric foundation. For instance, a perfect circle exhibits zero elongation and a roundness of one. Conversely, elongated structures, particularly those with strong (poloidal) elongation, tend to have reduced roundness, which is clearly reflected in the data.

Figure 8(d) presents the relationship between radial position and radial velocity. A positive correlation is observed indicating radially outwards acceleration. This finding is consistent with the observations reported in Fig. 5(c),(d) and Fig. 8(d) in Ref. 11, where outward radial acceleration of blobs was identified. One possible qualitative explanation of the acceleration is that blobs experience drag due to the background plasma density, which decreases radially outward in the SOL[29]. This decreasing background drag could allow blobs to accelerate more freely as they move outward. This result is consistent with the observations on Alcator C-Mod, where the radial velocity of blobs was also found to be increasing radially outwards in different plasma regimes[30].

The radial acceleration could be influenced by the shape or size change of the filaments, as well. Calculating the radial velocity contribution from the radial size change revealed a maximum 10% contribution to the overall radial velocity, which is insignificant in the scope of this study.

Figures 8(e) and (f) illustrate the dependence of the radial velocity on the minor and major semi-axes of the fitted ellipses, respectively. Both relationships exhibit significant negative correlation, indicating that blobs with larger semi-axes tend to propagate more slowly in the radial direction. This result resonates with the findings of Zweben et al in Ref. 11 where similar trends were found between the radial velocity and the poloidal size of blobs (see Fig. 8(c) and (d) therein). The underlying cause of this correlation requires further investigation, which lies beyond the scope of this manuscript. Interestingly, despite these correlations, blob area itself does not show a significant correlation with radial velocity, as indicated by the Pearson matrix. A similar trend was found by Birkenmeier et al in Ref.[31] where the blob's radial velocity scaled inversely to the radial size of the blobs, indicative of the sheath-connected blob regime. In lower single null TCV discharges reported by Tsui et al in Ref. 32, the normalized radial velocity, $\hat{v}$, scaled as $\hat{v} \sim \hat{a}^{1/2}$ with the normalized blob size $\hat{a}$ consistent with resistive-ballooning conditions. In our results on NSTX, the blob regimes in the discharges were not assessed individually, but based on the overall negative trend between the radial velocity and the blob sizes, it can be suspected that either the sheath-connected or the resistive X-point regime dominated the discharges.

In lower single-null discharges on TCV, Tsui et al.[32] reported that the normalized radial velocity scales with the square root of the normalized blob size, consistent with predictions for the resistive-ballooning regime. In the present NSTX analysis, individual blob regimes were not explicitly identified; however, the observed overall negative correlation between radial velocity and blob size suggests that blob dynamics in these discharges may be governed by either the sheath-connected or resistive X-point regime, both of which predict reduced radial velocities for larger structures.

In Figure 8(f), the negative correlation between the two quantities is not immediately apparent. When the correlation analysis is restricted to events with radial velocities in the range of [0, 1 km/s] and major semi-axes between [1 cm, 2 cm], a positive correlation results. However, a substantial number of events fall outside this peak region, contributing disproportionately to the overall trend and ultimately shifting the global correlation to a negative value.

Figure 8(g) presents the relationship between the area difference and the roundness difference parameters. A significant negative correlation is observed, implying that a decrease in blob area over time is typically accompanied by an increase in roundness, and vice versa. This result aligns with the earlier observation in Fig. 8(a), where convexity was negatively correlated with blob area.

Figure 8(h) displays the correlation between radial position and the major semi-axis of the fitted ellipse. A significant negative correlation is evident, suggesting that blobs located further radially outward in the SOL tend to exhibit smaller major semi-axes.

In addition to the parameter pairs with significant correlations, it is worth noting that some parameter pairs unexpectedly show no significant correlation. For example, previous studies reported a linear dependence between radial and angular velocities for ELM filaments[3,17]; however, no such relationship is observed for the SOL blobs. Furthermore, the expected angular velocity of the blobs is below the resolution of the analysis, indicating the possible absence of a coherent driving mechanism, such as the one present in ELM dynamics. In contrast to this, finite blob spin and a positive dependence and a scaling law between the radial velocity and blob rotation were reported from DIII-D by Molesworth et al in Ref. 33. Further investigation is needed to uncover the reason why we have not seen such behavior. D'Ippolito et al developed an analytical theory describing blob stability in relation to their internal rotation[34]. In the present analysis, no significant correlation was identified between blob spin and the convexity or solidity shape descriptors (quantifying the stability of their shape). Consequently, the experimental results reported here do not provide validation for the theoretical predictions.

Surprisingly, shape descriptors such as convexity, solidity, and roundness do not show significant correlation with the radial position. This suggests that blob shapes do not evolve in consistently or characteristically as they propagate radially outward through the SOL.

V. DISCUSSION

In this section, the results are discussed and, where applicable, related to existing physical models. Section V A examines the relationships between plasma and blob parameters, focusing on the identified correlations and observed trends. Section V C outlines the assumptions inherent in the analysis method and discusses the limitations of the implemented algorithms and their application. Finally, Section V D presents an outlook for future research directions and potential improvements to the methodology.

A. Dependence between blob and plasma parameters

Several methods were employed to investigate the relationships between blob properties and plasma parameters. In addition to traditional Pearson correlation coefficient analysis, we computed the mutual information metric[35] and the predictive power score[36] metrics, as well. These were evaluated between plasma parameters, characteristic of the 10 ms time window associated with blob analysis, and time-averaged blob parameters. The computations were carried out for three cases: shot-averaged, blob-averaged, and unaveraged blob data. Surprisingly, these metrics did not provide any conclusive insights. For completeness, these results are shown in the Appendix at Section VII.

Despite the inconclusive metric-based analysis, examination of parameter trends revealed notable associations between certain plasma parameters and blob characteristics. From the database, every blob-plasma parameter-pair trend was evaluated and the non-trivial ones having high coefficients of determination were chosen for further analysis. These results are presented in Fig. 9. Each subplot includes a linear regression along with its confidence interval, and the coefficient of determination (R^2) is indicated for each fit, as well. While the R^2 values remain relatively low, peaking at 0.65 for the trend between sound speed and blob tilt, these linear fits serve to highlight general trends rather than establish definitive quantitative relationships.

Figure 9(a) illustrates the relationship between the edge electron density and the minor semi-axis of the fitted ellipse characterizing the blob shape. A positive trend is observed, indicating that larger blobs are associated with higher edge densities. This observation is consistent with findings reported by Zweben in Ref. 11, where an increase in edge density corresponded to an increase in blob size. Similar trends were observed by Carralero et al in Ref. 37 where an investigation of collisionality revealed that filament sizes increased with higher collisionality, corresponding to elevated edge densities.

Figure 9(b) shows a positive trend between the line-integrated electron density and the tilt angle of the blob. Prior studies on the EAST tokamak have demonstrated that higher line-integrated electron densities are associated with increased blob lifetimes[38]. Based on this finding, the observed increase in tilt could be attributed to the blob remaining longer in the edge shear layer in higher-density plasmas, thus experiencing greater tilting. However, due to the limited spatial measure-

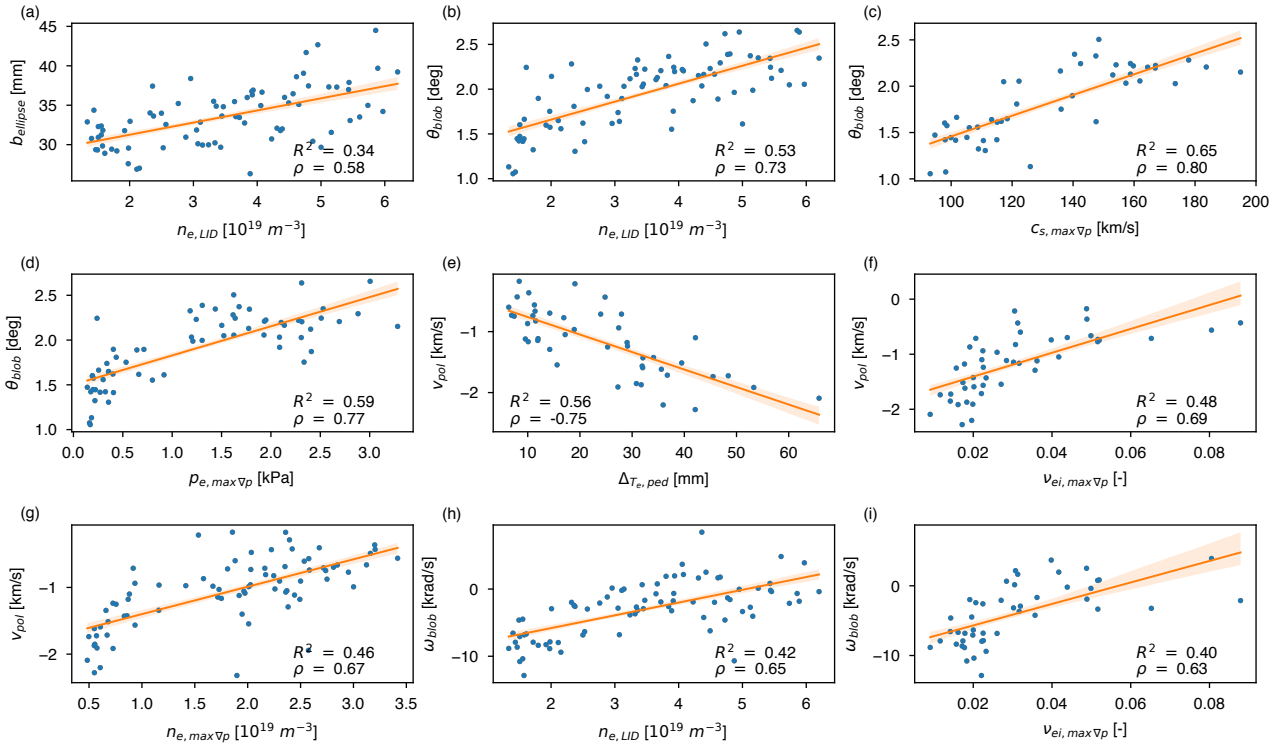

FIG. 9. Trends between selected plasma parameters during gas puff imaging (GPI) injection and the corresponding average blob parameters. Each subplot displays the Pearson correlation coefficient quantifying the linear relationship between the variables. The orange line indicates the best-fit linear regression, with the shaded region representing the 1σ confidence interval. (a) Line integrated electron density, $n_{e,LID}$, vs the minor semi-axis of the fitted ellipse, $b_{ellipse}$; (b) $n_{e,LID}$ vs the angle of the blob, θ_{blob}, with respect to horizontal; (c) the ion sound speed at the steepest electron pressure gradient, $c_{s,max\nabla p}$, vs θ_{blob}; (d) the electron pressure at the steepest electron pressure gradient, $p_{e,max\nabla p}$, vs θ_{blob}; (e) Electron temperature pedestal width, $\Delta_{T_e,ped}$, vs the poloidal velocity v_{pol}; (f) Electron-ion collisionality at the steepest electron pressure gradient, $\nu_{ei,\nabla p_{e,max}}$, vs v_{pol}; (g) The electron density at the steepest electron pressure gradient, $n_{e,\nabla p_{e,max}}$, vs v_{pol}; (h) $n_{e,LID}$ vs the angular velocity of the blobs ω_{blob}; (i) $\nu_{ei,\nabla p_{e,max}}$ vs ω_{blob}.

ment frame of the GPI diagnostic, direct lifetime measurements were not feasible; therefore, only speculative conclusions can be drawn regarding the causality of this trend.

Figure 9(c) presents a clear positive trend between the sound speed and the blob tilt angle. The sound speed was calculated from the electron temperature at the location of the maximum electron pressure gradient in the pedestal. One possible interpretation is that elevated electron temperatures, if accompanied by strong pressure gradients, may generate stronger sheared flows, leading to increased blob tilt. However, no statistically significant correlation was found between the absolute electron pressure and its gradient, suggesting that this mechanism cannot be conclusively verified. Notably, this parameter pair exhibits the highest coefficient of determination in this analysis, although an exact linear relationship remains unclear.

Figure 9(d) shows a positive trend between the blob tilt angle and the local electron pressure near the pressure gradient maximum. A previous study by Myra et al[39] has linked the strength of the pedestal pressure gradient to enhanced edge shear flows, which can induce blob tilt. In contrast, the present result suggests a potential direct influence of the local electron pressure on the tilt, a connection that has not been reported in earlier literature. As with the previous case, no significant correlation was found between the pressure gradient and the electron temperature, limiting the ability to confirm a shear-driven mechanism solely based on pressure.

Figure 9(e) shows the relationship between the width of the electron temperature pedestal and the poloidal velocity of the blob. The results indicate that blobs exhibit higher absolute poloidal velocities in plasmas with broader pedestals. A potential explanation is that narrower pedestals are typically associated with stronger edge shear layers, which may act to decelerate blobs. However, this interpretation remains speculative and warrants further investigation, ideally through detailed edge and scrape-off layer filament modeling.

Figure 9(f) shows a strong positive dependence between the poloidal velocity and the plasma collisionality (negative trend for the absolute poloidal velocity). Myra et al investigated the effects of collisionality on the radial blob velocity in an analytical model and found a positive dependence[40]; however, the poloidal velocity was not investigated. One speculative explanation for the observation could be that neoclassical viscosity increases with plasma collisionality, leading to increased damping of the blob dynamics, eventually leading to lower absolute poloidal velocities. N. Bisai has previously investi-

gated the effects of neoclassical viscosity on blob rotation in Ref.[41] but not its effect on the blob's poloidal velocity. It is noteworthy that while in our measurements the blob velocity was estimated in the SOL, the plasma collisionality was estimated at the position of the largest pressure gradient in the pedestal. In order to get a better estimate of the plasma collisionality in the SOL, the SOL measurement capabilities would need to be enhanced, which was unavailable at the time of the experiments.

Figure 9(g) shows the trend between the electron density at the location of the maximum pedestal pressure gradient and the poloidal velocity of the blob. Although a direct link between these parameters has not been explicitly explored in prior studies, some related observations can provide context. For example, Zweben et al reported in Ref. 8 that discharges with a higher fraction of blob coverage, i.e., a larger relative number of blobs in the GPI field of view, tend to exhibit lower edge electron densities and higher poloidal velocities. Additionally, Ref. 11 noted a relationship between blob velocity and relative density fluctuation amplitudes, though it did not explicitly analyze the impact of pedestal density. Following similar reasoning as in the interpretation of Fig. 9(e), it is plausible that higher pedestal densities correspond to steeper pressure gradients, which may in turn impede blob motion through increased damping or shear. However, confirming this hypothesis would require dedicated simulations of blob dynamics in the SOL, which lie beyond the scope of the present study.

Figure 9(h) illustrates the relationship between the line-integrated electron density and the angular velocity of the blobs. A clear positive trend is observed, supported by a relatively strong Pearson correlation coefficient of $\rho_{\mathrm{corr}} = 0.65$. This behavior may be interpreted in terms of increased collisionality, which is directly proportional to electron density in collisional plasma regimes. Higher collisionality can influence the internal dynamics of blobs, including their rotation, as discussed further below.

Figure 9(i) presents the dependence of blob angular velocity on pedestal collisionality. A positive trend is again observed, though the data exhibit considerable scatter, and no definitive functional relationship can be identified. Theoretical work by Myra et al in Ref. 42 examined blob vorticity within the framework of a Krook collision model but did not derive a direct dependence between vorticity and collisionality. More recently, Bisai investigated the effect of neoclassical viscosity on blob rotation and found that increased viscosity suppresses blob spin[41]. Our findings are qualitatively consistent with this result: in collisional regimes, plasma viscosity increases with collisionality, leading to enhanced damping of blob vorticity. Consequently, in lower collisionality plasmas, where viscous damping is weaker, blobs can sustain higher angular velocities. This trend underscores the potential importance of collisional viscosity in regulating filament rotation.

B. Analysis of blob regimes

Filaments in the scrape-off layer can behave differently based on the blob regimes they are in. The two region model defines the different blob regimes based on whether they are connected or disconnected from the divertor region[40]. In the sheath-connected regime (C_S), filaments are connected to the divertor plate, and the parallel current is driven by the mid-plane curvature which is limited by the sheath resistivity. In the ideal-interchange regime (C_I), the mid-plane curvature drive is balanced by perpendicular ion polarization currents enhanced by the X-point geometry. In the disconnected resistive X point regime, parallel currents are limited by divertor plasma resistivity. Finally, in the resistive ballooning regime (RB), the mid-plane drive is balanced by inertia at the mid-plane.

These regimes can be identified based on Λ, the dimensionless collisionality parameter, and Θ, the dimensionless blob size parameter. Θ is defined by $\hat{\delta}^{5/2}$ where $\hat{\delta} = \delta_b/\delta_*$. Here, $\delta_b = \sqrt{A/\pi}$ is the characteristic blob size where A is the blob's area. The normalizing factor, δ_*, is the characteristic blob scale defined by $\delta_* = \rho_s \left(\frac{L_{||}^2}{\rho_S R}\right)^{1/5}$ where $L_{||}$ is the parallel connection length, ρ_s is the sound Larmor radius, and R is the major radius. The parallel connection length is estimated from the mid-plane magnetic pitch angle and the geometrical distance between the mid-plane to the lower X-point and from there to the outer strike point. The rest of the parameters are estimated from the SOL plasma parameters from the equilibrium reconstruction and Thomson-scattering (TS) profile measurements.

Λ is defined as $\frac{\nu_{ei} L_{||}}{\Omega_e \rho_s}$ where ν_{ei} is the electron-ion collision frequency, and Ω_e is the electron gyro-frequency. Another parameter used for defining the blob regimes is the X-point magnetic fanning parameter, ε_x. The exact calculation for this can be found in Ref. 40. Here, we use an approximate value of $\varepsilon_x = 0.1$ calculated by Scotti et al in Ref. 43 for NSTX. The dimensionless parameters were calculated for each plasma discharge for averaged blob parameters and equilibrium reconstructions and TS measurements taken within the time range of the blob average. The results of the calculation are shown in Figure 10.

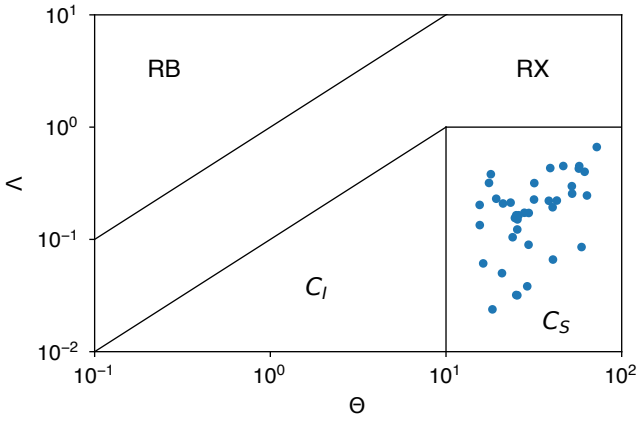

FIG. 10. Blob regime diagram for the four blob regimes of Resistive Ballooning (RB), Resistive X-point (RX), sheath-connected (C_S) and ideal interchange (C_I) regimes. The boundary between regions C_S and C_I was estimated from $\Theta = 1/\varepsilon_x \approx 10$. Theta is the dimensionless blob size calculated from the average blob size in each plasma discharge. Λ is the dimensionless collisionality parameter calculated for each discharge from the equilibrium reconstruction and the Thomson-scattering measurement.

Figure 10 shows the boundaries of the four blob regimes along with the dimensionless blob size and dimensionless collisionality data pairs for each discharge. The figure displays that all of the blob observations fall within the sheath-limited blob regime. To compare blob dynamics and morphology between the different blob regimes, the blob database would need to be extended with further discharges which is outside the scope of this paper.

To investigate how blobs are influenced by dimensionless collisionality and parallel connection lengths, their trends were investigated with linear regression. The calculation resulted relatively low R^2 values between them. Therefore, only the ones, which were higher than $R^2 > 0.2$, were plotted. In Ref. 40, connection between the dimensionless blob velocity and the dimensionless collisionality was investigated numerically and theoretically; therefore, the trends between them were plotted here, as well. The results are shown in Figure 11.

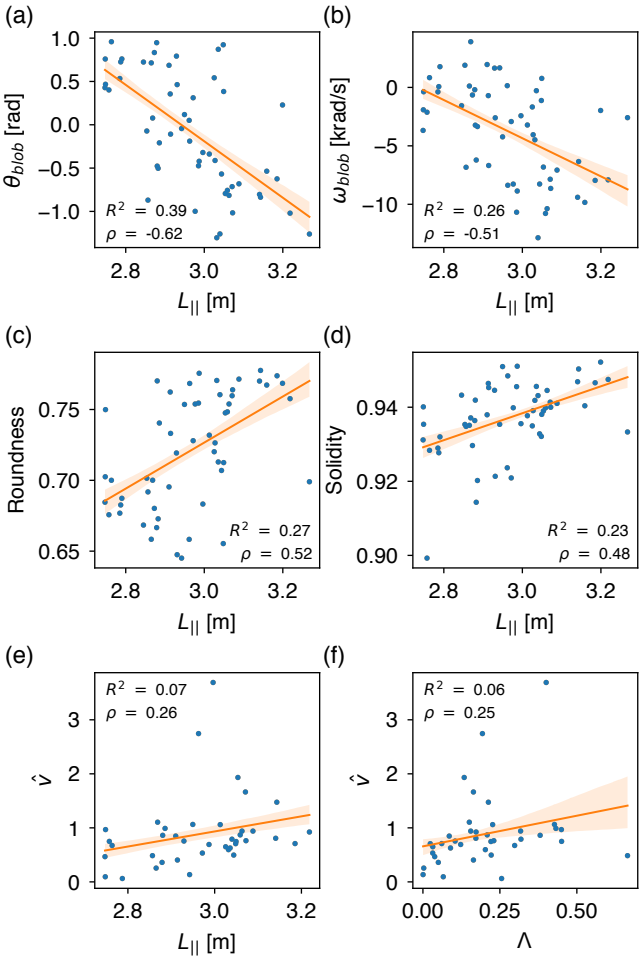

FIG. 11. Trends between dimensionless and blob parameters. (a) Parallel connection length ($L_{||}$) vs blob angle (θ_{blob}); (b) $L_{||}$ vs angular velocity (ω_{blob}); (c) $L_{||}$ vs roundness; (d) $L_{||}$ vs solidity; (e) $L_{||}$ vs dimensionless velocity ($\hat{v}$); (f) dimensionless collisionality (Λ) vs dimensionless velocity.

Fig. 11 (a) displays the trend between the connection length and the blob angle. Significant negative trend is seen between these two parameters fortified by the relatively high -0.62 correlation coefficient. The coefficient of determination is 0.39 which is higher than for the rest of the parameter pairs but does not indicate a clear linear relationship between the parameters.

The negative trend can be speculatively explained by geometrical effects. The two-dimensional plane of the quasi-2D GPI gas cloud's angle with respect to the line-of-sight is independent of the magnetic configuration. Shorter connection lengths are a result of higher magnetic field pitch angles which make the blob angle with respect to the gas cloud distorted. The lower the connection length, the higher the poloidal field is resulting in a higher pitch angle at the measurement location. Should a blob enter the observation area with a finite angle, its apparent angle will be higher due to the distortion. This argument does not explain the large range of observed angles, though, and would only work in a narrow range of angles.

Fig. 11 (b) shows the trend between the parallel connection length and the spin (angular velocity) of the blob. Significant negative correlation, $\rho = -0.51$ is found between these parameters, however, the negative trend is not as apparent as in (a) due to a large scatter in the data. The coefficient of determination is also low at $R^2 = 0.26$ meaning that no clear linear relationship exists between these two parameters.

Positive trends are seen between the parallel connection length and the roundness and solidity shape descriptors in Fig. 11 (c) and (d). Similar correlation coefficients and coefficients of determination are found between them. The latter coefficients are low meaning that no clear linear relationship is found between them. The high correlation coefficient however indicates, that plasmas with higher connection lengths exhibit rounder and more solid blobs.

Fig. 11 (e) and (f) display the trends between the parallel connection length, the dimensionless collisionality and the dimensionless blob velocity. The dimensionless blob velocity is calculated from $\hat{v} = v_{rad}/v_*$ where $v_* = c_s(\frac{a_*}{R})^{1/2}$ and $a_* = \frac{\rho_S^{4/5} L_{||}^{2/5}}{R^{1/5}}$ Positive trend is seen between the parallel connection length and $\hat{v}$, and the dimensionless collisionality and $\hat{v}$, as well. Even though the correlation coefficients are relatively low, the positive trend aligns well with the blob theory presented by Myra et al in Ref. 40. The coefficient of determination is close to zero indicating the lack of linear relationship between the parameters.

C. Assumptions and limitations of the analysis

Several assumptions and limitations underlie the methodologies employed in this study. These pertain to the diagnostic constraints of the GPI system, the resolution of Thomson scattering measurements, and the performance of the image segmentation and structure tracking algorithms. This section outlines these considerations to contextualize the results and guide future improvements.

1. *Limitations of the GPI diagnostic*

The GPI diagnostic operates by measuring light emission resulting from the interaction between the neutral gas and the plasma. In the analysis, the neutral gas cloud is assumed to be quasi-two-dimensional. However, due to the $\sim 22^\circ$ half-cone angle of the gas injection, the gas cloud develops considerable depth by the time it reaches the separatrix. This volumetric spread can degrade the effective spatial resolution, especially if the line-of-sight of the diagnostic is not well-aligned with the magnetic field lines. Although the NSTX GPI's LOS is approximately aligned with the magnetic field, variations in magnetic configuration between discharges can introduce misalignment, leading to degradation in spatial resolution.

It is important to note that the injected gas puff imposes limitations on the radial observation range of filaments. Closer to the core plasma, the neutral density is significantly attenuated due to increased ionization and collisional excitation in the higher-density region, which reduces the available neutrals for light emission. As a result, blob detection within more than a few centimeters away from the separatrix is constrained by a low signal-to-noise ratio. Outside the confined region, in the far SOL, the neutral density remains high near the gas injection manifold; however, the background plasma density is low, leading to weak background emission. Despite this, filaments with locally elevated density and temperature can still excite the neutrals sufficiently, enabling their detection even in the far SOL.

2. *Limitations of the blob database*

The blob database was compiled from 86 discharges from the 2010 NSTX experimental campaign, encompassing both low- and high-confinement (L-mode and H-mode) plasma regimes. The plasma regimes affect certain dynamics of blobs as it was shown in previous studies[2,15]. Blob dynamics are influenced by the local SOL conditions, particularly the electron temperature, which determines whether filaments evolve in the sheath-limited or conduction-limited transport regime[44].

In the present study, the dependence of blob dynamics and morphology on the overall confinement regime or local transport regime was not explicitly analyzed. Instead, the focus was on characterizing the general morphological and dynamical features of blobs in a regime-agnostic manner. It's noteworthy to mention that a preliminary comparison of blob properties in L-mode and H-mode plasmas indicated no substantial differences in parameter distributions, correlations, or observed trends. A detailed analysis of these regime-dependent effects is beyond the scope of this work but is planned for future investigation.

3. *Limitations of Thomson scattering profile fits*

The dependency analysis between blob and plasma parameters in Section IV B 3 relies on Thomson scattering measurements to extract pedestal density and temperature profiles. In spherical tokamaks, this presents a challenge: pedestal widths are typically narrow (on the order of 1–2 cm), while the spatial resolution of the TS system is limited. As a result, accurate fitting of the pedestal gradients is constrained, introducing uncertainty in the extracted plasma parameters. Planned upgrades to the NSTX-U TS system, including improved digitizers and enhanced spatial resolution, will allow for more precise characterization of pedestal structures in future experiments.

4. *Image segmentation and tracking algorithm performance*

The blob characterization relies on a complex multi-stage image processing pipeline (Fig. 3). This method relies on several assumptions as follows.

- Background normalization: the raw GPI image frames are normalized using a 1 kHz low-pass filter. This assumes that the background gas evolves on timescales much slower than 1 ms, while blobs evolve much faster. This assumption holds in both L-mode and H-mode regimes; however, during edge localized mode events, the background can be perturbed on sub-ms timescales. To mitigate this, time windows containing ELMs were excluded from the analysis.

- Thresholding techniques: two approaches, intensity thresholding and Otsu's method, are used to separate blobs from the background. Both methods rely on the assumption that blob emission is significantly more intense than the background. This is valid only during peak emission periods when the neutral cloud is most dense. The analysis is restricted to these periods, thereby justifying this assumption.

- Watershed segmentation: structure identification is performed using the watershed algorithm, which assumes each blob has a single local intensity maximum with a monotonically decreasing intensity profile. This assumption is generally valid due to the approximately Gaussian nature of blob density distributions. However, occasional blob merging or splitting (which occurs in about 5% of the frames with blobs in the GPI videos) may result in over- or under-segmentation. Given its low frequency, this limitation is not expected to significantly impact statistical results.

- Tracking via intersection over union: blobs are tracked between frames by calculating the IoU, assuming spatial overlap between consecutive observations. Given the 2.5 μs frame rate of the GPI diagnostic and the relatively slow dynamics of blob motion, this is a reasonable assumption. However, if structure identification fails in a single frame, the blob may be erroneously split into two distinct entities in the tracking phase. This limitation has a negligible impact on averaged parameter statistics but constrains analysis of properties such as blob lifetime, birth-rate, or interaction dynamics. These analyses are deferred to future work.

5. Temporal Resolution Mismatch in Parameter Correlation

Correlations between plasma parameters and blob properties are constrained by the temporal mismatch between diagnostics. Plasma parameters are typically measured at 16 ms intervals using TS on NSTX, whereas blob parameters are derived from GPI data sampled at 2.5 μs. In this study, it is assumed that the plasma profiles remain stationary over the $\sim$10 ms time window used for blob analysis. This assumption is valid within selected time intervals representing steady-state plasma conditions. However, the lack of higher time resolution TS data limits the precision of the correlation analysis. Future studies incorporating faster TS systems will be essential to resolve this limitation.

D. Outlook for future research

This study analyzed legacy NSTX data from 2010, a period during which the gas puff imaging (GPI) diagnostic operated at optimal performance and the plasma conditions were ideal for blob observation. With NSTX-U scheduled to resume operation in 2026, future experiments will offer new opportunities to expand the blob database using higher-performance discharges. In parallel, diagnostic capabilities are expected to significantly improve. Notably, the Thomson scattering system will offer enhanced temporal and spatial resolution, enabling more precise measurements of the electron density and temperature pedestal profiles. This improvement will support more accurate profile fitting and facilitate higher-fidelity analysis of the dependencies between blob dynamics and edge plasma parameters.

Estimating blob shape parameters from GPI data remains a challenge due to the finite extent of the neutral gas cloud and the complex three-dimensional geometry formed by the relative orientations of the gas cloud, magnetic field lines, and diagnostic line-of-sight. One promising avenue is the development of a reduced synthetic GPI diagnostic model coupled with the computation of a local fluctuation-response matrix. Inverting this matrix and applying it to experimental data could allow reconstruction of the local electron density fluctuations, thus providing more accurate estimates of filament shape and structure[45]. On Alcator C-Mod, the DEGAS 2 Monte Carlo neutral transport code was employed to develop a synthetic GPI diagnostic[46], with the resulting simulations subsequently used to validate the XGC gyrokinetic full-f code[47]. For NSTX, the feasibility of applying DEGAS 2 to generate a fast and accurate synthetic GPI diagnostic remains to be evaluated. In addition, a realistic observation module will need to be incorporated into the synthetic diagnostic framework to model the specific optical characteristics of the NSTX GPI system.

Since the implementation of the watershed-based segmentation algorithm used in this work, significant progress has been made in the field of image segmentation. For instance, region-based convolutional neural networks (Mask R-CNNs) have shown promising results in segmenting structures in GPI images[48]. While these deep learning models require substantial supervised training and computational resources, their application to filament detection in future NSTX-U data could be explored to assess their robustness and accuracy compared to traditional methods. The application of such advanced methods was beyond the scope of this work, but remains a compelling direction for future research.

Some of the trends observed in this study, particularly those concerning blob velocity and shape dependence on edge plasma parameters, cannot yet be fully explained by existing theoretical models. To gain a deeper understanding, comprehensive numerical simulations of scrape-off layer turbulence in relevant plasma regimes will be essential. Such simulations could be performed using advanced gyro-kinetic codes, such as GKEYLL[49] or XGC[47], which can resolve filamentary dynamics in realistic spherical tokamak geometries. GENE-X is also a strong candidate for SOL turbulence simulation

studies, as it is capable of modeling plasmas with realistic X-point geometries[50]. Recent developments, including the implementation of a spectral representation of velocity space, have resulted in substantial computational speed-ups[51], further enhancing its suitability for large-scale edge and SOL turbulence investigations. Fluid codes such as GBS[52,53] and SOLT[54] were also compared to GPI measurements before and could be used again to gain understanding of the results presented here.

VI. SUMMARY

Filamentary structures in the scrape-off layer of tokamak plasmas are a major source of intermittent heat and particle transport, thereby degrading overall plasma confinement. Understanding the dynamics of these filaments is critical for the success of future fusion reactors such as ITER.

To analyze blobs, a novel image analysis workflow was developed based on an enhanced watershed segmentation algorithm. This method enables robust identification, segmentation, and tracking of filaments in gas-puff imaging data. Tracked structures were further analyzed using geometric shape descriptors, including convexity, roundness, solidity, and total curvature.

A comprehensive database was compiled from 86 discharges, yielding 11075 individual identified blobs. Statistical analysis of their shape descriptors revealed that filament area follows a positively skewed distribution, while the time derivative of the area approximates a Gaussian distribution. Filament alignment angles peaked at 78 degrees, indicating a predominantly poloidal orientation. The distribution of angular velocities was centered around zero, contrasting results of ELM filament analysis, where significant spinning was found in previous research. Roundness of blobs peaked near 0.82 but exhibited substantial variability, reaching values as low as 0.25. This is a result of the elongation of blobs in the poloidal direction. The time derivatives of roundness and curvature exhibited distributions with a peak at zero, indicating that blobs do not change their shape characteristically during their time evolution.

Two-dimensional joint distribution analyses between blob parameters uncovered several significant dependencies. A strong negative correlation between area and convexity indicated that larger filaments tend to assume more concave and potentially unstable shapes. Consistent with behavior observed in edge localized mode (ELM) filaments, a positive correlation between filament radial position and radial velocity was found, potentially due to decreasing background plasma density, which reduces the retaining force on larger blobs. No clear dependency was observed between angular velocity and other shape parameters.

To further explore the physics of blob dynamics, cross-analysis was performed between blob properties and background plasma parameters. While metrics such as cross-correlation, mutual information, and predictive power score did not uncover previously unseen relationships, trend analysis revealed interesting dependencies. Notably, a near-linear relationship was observed between line-integrated electron density and blob angular velocity, and between sound speed and blob tilt angle, as well.

Future work will build on these findings using new data from the upcoming NSTX-U campaigns. Development of a synthetic GPI diagnostic is also planned to investigate the impact of 3D observational geometry on apparent filament shape. Finally, future work will include systematic comparisons of experimental observations with first-principles simulations, including gyrokinetic codes such as GKEYLL and XGC, as well as fluid turbulence models such as GBS and SOLT, in order to obtain deeper physical insight into filament dynamics.

ACKNOWLEDGEMENT

The authors thank S. J. Zweben for his tremendous work on the GPI diagnostic. This work was supported by U.S. DOE Contract No. DE-AC02-09CH11466 (PPPL). The United States Government retains a non-exclusive, paid-up, irrevocable, world-wide license to publish or reproduce the published form of this manuscript, or allow others to do so, for United States Government purposes.

AUTHOR DECLARATIONS

Conflict of interest

The authors have no conflict of interest to disclose.

Data availability

The data that support the findings of this study are openly available under Ref. 16 [to be changed before the final submission].

Appendices

VII. METRICS CALCULATED BETWEEN BLOB AND PLASMA PARAMETERS

During the analysis, three different metrics were calculated to uncover the relationship between plasma and blob parameters: correlation coefficient, predictive power score and mutual information. The results of this calculation were inconclusive and no new physics could be uncovered based on them. However, they are shown for the potential interest of the reader.

Fig. 12 shows the Pearson correlation coefficients calculated between the shot-averaged blob parameters and the estimated profile parameters and with the blob-blob and the plasma-plasma coefficients. Relatively high correlation can be seen between all of the parameters which is a result of the

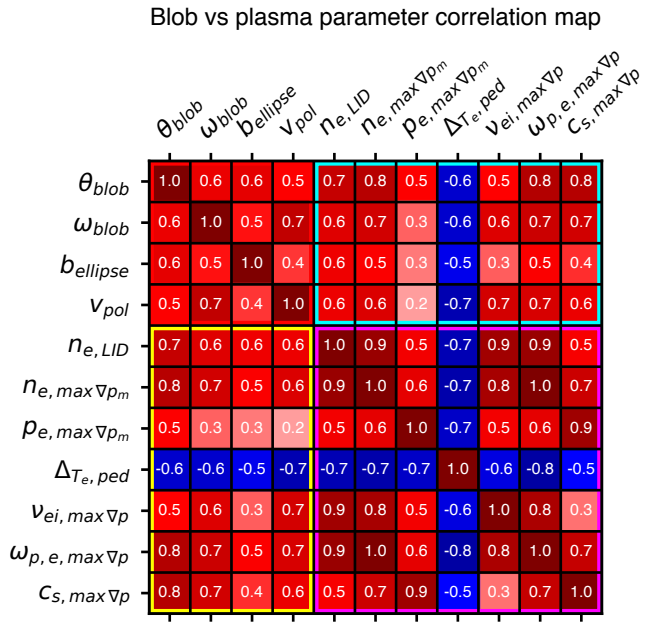

FIG. 12. Correlation coefficients calculated between shot averaged blob parameters and plasma profile parameters. Blob-blob (red square) and plasma-plasma (magenta square) parameter correlations are also shown.

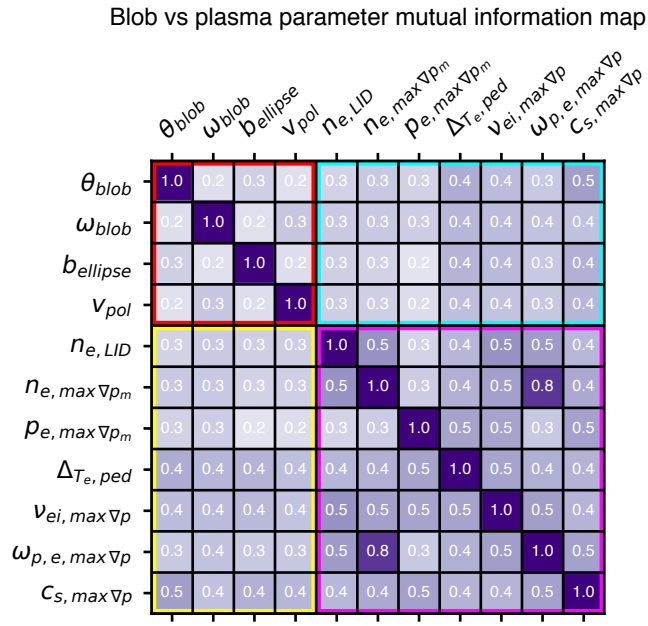

FIG. 13. Mutual information matrix calculated between shot averaged blob parameters and plasma profile parameters. Blob-blob (red square) and plasma-plasma (magenta square) parameter mutual information are also shown.

low statistics due to the low temporal resolution of the profile diagnostics. Correlation analysis of blob-averaged and unaveraged data were also attempted. Blob-average means that for every identified blob, the estimated parameters were averaged resulting in a number of data points equal to the number of identified blobs. Unaveraged means that data at each timepoint of each identified blob was considered as separate. To calculate the correlation coefficients between these extended number of data-points and the plasma profile parameters, the latter had to be interpolated with the nearest neighbor method. This analysis, however, did not reveal further insights into the physics of blobs.

Fig. 13 shows the mutual information (MI) calculation between the blob and plasma parameters. This metric is symmetric similar to the correlation coefficient. Mutual information quantifies the amount of information obtainable from one random variable about another random variable[35]. Similar MI values are observed between all blob-plasma parameter pairs in the range of 0.2 - 0.5. This analysis did not reveal a clear connection between the blob and the plasma parameters. High mutual information values can only be seen between plasma-plasma parameter MI values where the parameters are a function of each other.

Fig. 14 shows the predictive power score (PPS between the shot-averaged estimated blob parameters and the plasma parameters. Note, that this metric is not symmetric unlike the Pearson-correlation coefficient or the mutual information metrics. Only low values of PPS are found for blob-plasma and plasma-blob calculations. High PPS values are present in the plasma-plasma parameter analysis for parameter pairs that are a function of each other, e.g., the plasma frequency and the plasma density.

These cross-parameter analyses did not reveal any novel dependency between the plasma and the blob parameters. One reason for this negative result is that the number of plasma profiles that were used for the analysis was low, only one for each time range. Should another means for fast profile measurement be available, e.g., alkali beam emission spectroscopy for fast absolute electron density profile measurements[55], a more detail investigation can be done.

[1] S. I. Krasheninnikov, D. A. D'Ippolito, and J. R. Myra, "Recent theoretical progress in understanding coherent structures in edge and sol turbulence," Journal of Plasma Physics **74**, 679–717 (2008).
[2] D. A. D'Ippolito, J. R. Myra, and S. J. Zweben, "Convective transport by intermittent blob-filaments: Comparison of theory and experiment," Physics of Plasmas **18**, 060501 (2011).
[3] M. Lampert, A. Diallo, J. R. Myra, and S. J. Zweben, "Internal rotation of ELM filaments on NSTX," Physics of Plasmas **29**, 102502 (2022).
[4] J. A. Boedo, D. L. Rudakov, R. A. Moyer, G. R. McKee, R. J. Colchin, M. J. Schaffer, P. G. Stangeby, W. P. West, S. L. Allen, T. E. Evans, R. J. Fonck, E. M. Hollmann, S. Krasheninnikov, A. W. Leonard, W. Nevins, M. A. Mahdavi, G. D. Porter, G. R. Tynan, D. G. Whyte, and X. Xu, "Transport by intermittency in the boundary of the DIII-D tokamak," Physics of Plasmas **10**, 1670–1677 (2003).

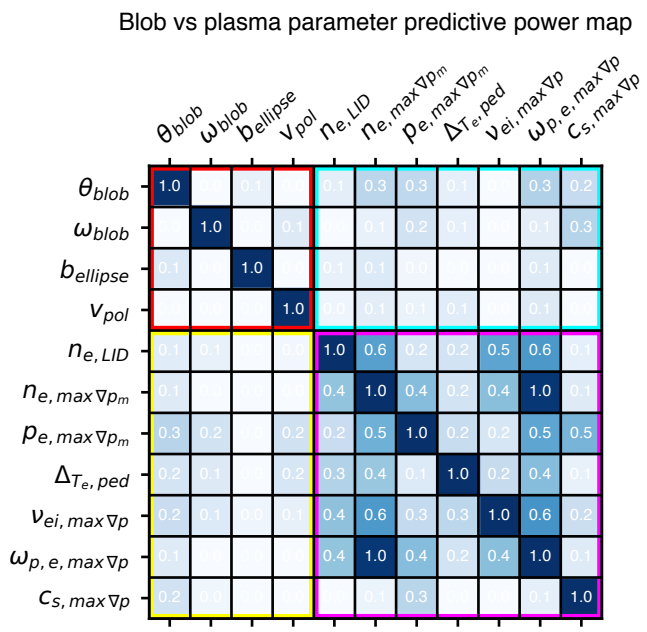

FIG. 14. Predictive power score matrix calculated between shot averaged blob parameters and plasma profile parameters. Blob-blob (red square) and plasma-plasma (magenta square) parameter scores are also shown. Notice that the predictive power score matrix is not symmetrical unlike the correlation and mutual information matrices.

[5] S. Zweben, W. Davis, S. Kaye, J. Myra, R. Bell, B. LeBlanc, R. Maqueda, T. Munsat, S. Sabbagh, Y. Sechrest, and D. S. and, "Edge and SOL turbulence and blob variations over a large database in NSTX," Nuclear Fusion **55**, 093035 (2015).

[6] J. M. Dewhurst, B. Hnat, N. Ohno, R. O. Dendy, S. Masuzaki, T. Morisaki, and A. Komori, "Statistical properties of edge plasma turbulence in the large helical device," Plasma Physics and Controlled Fusion **50**, 095013 (2008).

[7] T. A. Carter, "Intermittent turbulence and turbulent structures in a linear magnetized plasma," Physics of Plasmas **13**, 010701 (2006).

[8] S. J. Zweben, S. Banerjee, N. Bisai, A. Diallo, M. Lampert, B. LeBlanc, J. R. Myra, and D. A. Russell, "Correlation between the relative blob fraction and plasma parameters in NSTX," Physics of Plasmas **29**, 012505 (2022).

[9] G. Fuchert, D. Carralero, P. Manz, U. Stroth, E. Wolfrum, and A. U. Team, "Towards a quantitative prediction of the blob detection rate," Plasma Physics and Controlled Fusion **58**, 054006 (2016).

[10] N. Bisai, S. Banerjee, S. Zweben, and A. Sen, "Experimental validation of universal plasma blob formation mechanism," Nuclear Fusion **62**, 026027 (2022).

[11] S. J. Zweben, J. R. Myra, W. M. Davis, D. A. D'Ippolito, T. K. Gray, S. M. Kaye, B. P. LeBlanc, R. J. Maqueda, D. A. Russell, and D. P. S. and, "Blob structure and motion in the edge and SOL of NSTX," Plasma Physics and Controlled Fusion **58**, 044007 (2016).

[12] S. J. Zweben, M. Lampert, and J. R. Myra, "Temporal structure of blobs in NSTX," Physics of Plasmas **29**, 072504 (2022).

[13] S. J. Zweben, D. P. Stotler, F. Scotti, and J. R. Myra, "Two-dimensional turbulence cross-correlation functions in the edge of NSTX," Physics of Plasmas **24**, 102509 (2017).

[14] M. Ono, S. Kaye, Y.-K. Peng, G. Barnes, W. Blanchard, M. Carter, J. Chrzanowski, L. Dudek, R. Ewig, D. Gates, R. Hatcher, T. Jarboe, S. Jardin, D. Johnson, R. Kaita, M. Kalish, C. Kessel, H. Kugel, R. Maingi, R. Majeski, J. Manickam, B. McCormack, J. Menard, D. Mueller, B. Nelson, B. Nelson, C. Neumeyer, G. Oliaro, F. Paoletti, R. Parsells, E. Perry, N. Pomphrey, S. Ramakrishnan, R. Raman, G. Rewoldt, J. Robinson, A. Roquemore, P. Ryan, S. Sabbagh, D. Swain, E. Synakowski, M. Viola, M. Williams, J. Wilson, and N. Team, "Exploration of spherical torus physics in the NSTX device," Nuclear Fusion **40**, 557–561 (2000).

[15] G. Fuchert, G. Birkenmeier, D. Carralero, T. Lunt, P. Manz, H. W. Müller, B. Nold, M. Ramisch, V. Rohde, U. Stroth, and the ASDEX Upgrade Team, "Blob properties in l- and h-mode from gas-puff imaging in asdex upgrade," Plasma Physics and Controlled Fusion **56**, 125001 (2014).

[16] M. Lampert, A. Diallo, and J. Myra, "Evolution of intermittent filaments in the scrape-off layer of nstx," https://dataspace.princeton.edu/handle/88435/dsp011v53k0334 (2024).

[17] M. Lampert, A. Diallo, J. R. Myra, and S. J. Zweben, "Dynamics of filaments during the edge-localized mode crash on NSTX," Physics of Plasmas **28**, 022304 (2021).

[18] T. Farley, N. R. Walkden, F. Militello, M. Sanna, J. Young, S. S. Silburn, J. Harrison, L. Kogan, I. Lupelli, S. S. Henderson, A. Kirk, and J. W. Bradley, "Filament identification in wide-angle high speed imaging of the mega amp spherical tokamak," Review of Scientific Instruments **90**, 093502 (2019).

[19] D. M. Jiménez-Bravo, Á. Lozano Murciego, A. Sales Mendes, H. Sánchez San Blás, and J. Bajo, "Multi-object tracking in traffic environments: A systematic literature review," Neurocomputing **494**, 43–55 (2022).

[20] J. Žunić, eng"Shape descriptors for image analysis," Zbornik Radova , 5–38 (2012).

[21] M. Lampert, "FLAP: Fusion Library of Analysis Programs, NSTX repository," `https://github.com/fusion-flap/flap_nstx/tree/RSI_2022_version`.

[22] R. Kube, O. Garcia, B. LaBombard, J. Terry, and S. Zweben, "Blob sizes and velocities in the alcator c-mod scrape-off layer," Journal of Nuclear Materials **438**, S505–S508 (2013), proceedings of the 20th International Conference on Plasma-Surface Interactions in Controlled Fusion Devices.

[23] N. Offeddu, C. Wüthrich, W. Han, C. Theiler, T. Golfinopoulos, J. L. Terry, E. Marmar, A. Ravetta, and G. Van Parys, "Analysis techniques for blob properties from gas puff imaging data," Review of Scientific Instruments **94**, 033512 (2023), https://pubs.aip.org/aip/rsi/article-pdf/doi/10.1063/5.0133506/16796367/033512_1_online.pdf.

[24] L. Najman and M. Schmitt, "Watershed of a continuous function," Signal Processing **38**, 99–112 (1994).

[25] S. F. Frisken, R. N. Perry, A. P. Rockwood, and T. R. Jones, "Adaptively sampled distance fields: A general representation of shape for computer graphics," in *Proceedings of the 27th Annual Conference on Computer Graphics and Interactive Techniques*, SIGGRAPH '00 (ACM Press/Addison-Wesley Publishing Co., USA, 2000) p. 249–254.

[26] N. Otsu, "A threshold selection method from gray-level histograms," IEEE Transactions on Systems, Man, and Cybernetics **9**, 62–66 (1979).

[27] H. W. Kuhn, "The hungarian method for the assignment problem," Naval Research Logistics Quarterly **2**, 83–97 (1955).

[28] B. Braden, "The surveyor's area formula," The College Mathematics Journal **17**, 326–337 (1986), https://doi.org/10.1080/07468342.1986.11972974.

[29] K. Bodi, S. I. Krasheninnikov, and A. I. Smolyakov, "Blob dynamics in an inhomogeneous plasma," Physics of Plasmas **15**, 102304 (2008).

[30] A. Helgeland, J. Losada, J. Terry, and O. Garcia, "Blob velocities and sizes in the alcator c-mod scrape-off layer for ohmic and high confinement mode plasmas," Nuclear Materials and Energy **43**, 101930 (2025).

[31] G. Birkenmeier, F. M. Laggner, M. Willensdorfer, T. Kobayashi, P. Manz, E. Wolfrum, D. Carralero, R. Fischer, B. Sieglin, G. Fuchert, U. Stroth, and the ASDEX upgrade team, "Magnetic field dependence of the blob dynamics in the edge of asdex upgrade l-mode plasmas," Plasma Physics and Controlled Fusion **56**, 075019 (2014).

[32] C. K. Tsui, J. A. Boedo, J. R. Myra, B. Duval, B. Labit, C. Theiler, N. Vianello, W. A. J. Vijvers, H. Reimerdes, S. Coda, O. Février, J. R. Harrison, J. Horacek, B. Lipschultz, R. Maurizio, F. Nespoli, U. Sheikh, K. Verhaegh, N. Walkden, T. Team, and E. M. Team, "Filamentary velocity scaling validation in the tcv tokamak," Physics of Plasmas **25**, 072506 (2018), https://pubs.aip.org/aip/pop/article-pdf/doi/10.1063/1.5038019/14763864/072506_1_online.pdf.

[33] S. C. Molesworth, J. A. Boedo, C. K. Tsui, R. Perillo,

and D. L. Rudakov, "Filamentary velocity scaling validation and spin dynamics in the diii-d tokamak," Physics of Plasmas **31**, 042515 (2024), https://pubs.aip.org/aip/pop/article-pdf/doi/10.1063/5.0195025/19896404/042515_1_5.0195025.pdf.

[34]D. A. D'Ippolito, J. R. Myra, D. A. Russell, and G. Q. Yu, "Rotational stability of plasma blobs," Physics of Plasmas **11**, 4603–4609 (2004), https://pubs.aip.org/aip/pop/article-pdf/11/10/4603/19190898/4603_1_online.pdf.

[35]N. S. Tzannes and J. P. Noonan, "The mutual information principle and applications," Information and Control **22**, 1–12 (1973).

[36]F. Wetschoreck, T. Krabel, and S. Krishnamurthy, "8080labs/ppscore: zenodo release," (2020).

[37]D. Carralero, P. Manz, L. Aho-Mantila, G. Birkenmeier, M. Brix, M. Groth, H. W. Müller, U. Stroth, N. Vianello, and E. Wolfrum (ASDEX Upgrade team and JET Contributors and EUROfusion MST1 Team), "Experimental validation of a filament transport model in turbulent magnetized plasmas," Phys. Rev. Lett. **115**, 215002 (2015).

[38]P. Wand, G. Hu, N. Yan, G. Xu, L. Meng, Z. Lu, L. yu, M. Jia, Y. Wang, L. Chen, H. Lan, X. Liu, M. Wu, and L. Wang, "Experimental investigation of scrape-off layer blob high density transition in l-mode plasmas on east," Plasma Science and Technology **24**, 075103 (2022).

[39]J. Myra, W. Davis, D. D'Ippolito, B. LaBombard, D. Russell, J. Terry, and S. Zweben, "Edge sheared flows and the dynamics of blob-filaments," Nuclear Fusion **53**, 073013 (2013).

[40]J. R. Myra, D. A. Russell, and D. A. D'Ippolito, "Collisionality and magnetic geometry effects on tokamak edge turbulent transport. i. a two-region model with application to blobs," Physics of Plasmas **13**, 112502 (2006).

[41]N. B. and, "On spin of plasma blob in edge and scrape-off layer regions of a tokamak," Radiation Effects and Defects in Solids **179**, 945–953 (2024).

[42]J. R. Myra, J. Cheng, and S. E. Parker, "Dynamics of rapidly spinning blob-filaments: Fluid theory with a parallel kinetic extension," Physics of Plasmas **30**, 072302 (2023).

[43]F. Scotti, S. Zweben, J. Myra, R. Maqueda, and V. Soukhanovskii, "Disconnection of scrape off layer turbulence between the outer midplane and divertor target plate in nstx," Nuclear Fusion **60**, 026004 (2019).

[44]J. R. Myra, D. A. D'Ippolito, D. P. Stotler, S. J. Zweben, B. P. LeBlanc, J. E. Menard, R. J. Maqueda, and J. Boedo, "Blob birth and transport in the tokamak edge plasma: Analysis of imaging data," Physics of Plasmas **13**, 092509 (2006), https://pubs.aip.org/aip/pop/article-pdf/doi/10.1063/1.2355668/14748906/092509_1_online.pdf.

[45]M. Lampert, "Absolute electron density fluctuation reconstruction for two-dimensional hydrogen beam emission spectroscopy," Review of Scientific Instruments **94**, 123501 (2023).

[46]D. P. Stotler, S. Ku, S. J. Zweben, C. S. Chang, R. M. Churchill, and J. L. Terry, "Examination of synthetic gas puff imaging diagnostic data from a gyrokinetic turbulence code," Physics of Plasmas **27**, 062512 (2020), https://pubs.aip.org/aip/pop/article-pdf/doi/10.1063/5.0002876/16049929/062512_1_online.pdf.

[47]R. Hager, S. Ku, A. Y. Sharma, C. S. Chang, R. M. Churchill, and A. Scheinberg, "Electromagnetic total-f algorithm for gyrokinetic particle-in-cell simulations of boundary plasma in xgc," Physics of Plasmas **29**, 112308 (2022).

[48]W. Han, R. A. Pietersen, R. Villamor-Lora, M. Beveridge, N. Offeddu, T. Golfinopoulos, C. Theiler, J. L. Terry, E. S. Marmar, and I. Drori, "Tracking blobs in the turbulent edge plasma of a tokamak fusion device," Scientific Reports **12**, 18142 (2022).

[49]T. N. Bernard, F. D. Halpern, M. Francisquez, G. W. Hammett, and A. Marinoni, "Plasma edge and scrape-off layer turbulence in gyrokinetic simulations of negative triangularity plasmas," Plasma Physics and Controlled Fusion **66**, 115017 (2024).

[50]D. Michels, A. Stegmeir, P. Ulbl, D. Jarema, and F. Jenko, "Gene-x: A full-f gyrokinetic turbulence code based on the flux-coordinate independent approach," Computer Physics Communications **264**, 107986 (2021).

[51]P. Ulbl, A. Stegmeir, D. Told, G. Merlo, K. Zhang, and F. Jenko, "Simulations of edge and sol turbulence in diverted negative and positive triangularity plasmas," (2025), arXiv:2504.00475 [physics.plasm-ph].

[52]F. D. Halpern, J. L. Terry, S. J. Zweben, B. LaBombard, M. Podesta, and P. Ricci, "Comparison of 3d flux-driven scrape-off layer turbulence simulations with gas-puff imaging of alcator c-mod inner-wall limited discharges," Plasma Physics and Controlled Fusion **57**, 054005 (2015).

[53]F. D. Halpern, B. LaBombard, J. L. Terry, and S. J. Zweben, "Outer midplane scrape-off layer profiles and turbulence in simulations of alcator c-mod inner-wall limited discharges," Physics of Plasmas **24**, 072502 (2017), https://pubs.aip.org/aip/pop/article-pdf/doi/10.1063/1.4989705/16000428/072502_1_online.pdf.

[54]D. A. Russell, J. R. Myra, D. A. D'Ippolito, T. L. Munsat, Y. Sechrest, R. J. Maqueda, D. P. Stotler, S. J. Zweben, and T. N. Team, "Comparison of scrape-off layer turbulence simulations with experiments using a synthetic gas puff imaging diagnostic," Physics of Plasmas **18**, 022306 (2011), https://pubs.aip.org/aip/pop/article-pdf/doi/10.1063/1.3553024/15696827/022306_1_online.pdf.

[55]M. Lampert, G. Anda, A. Czopf, G. Erdei, D. Guszejnov, Á. Kovácsik, G. I. Pokol, D. Réfy, Y. U. Nam, and S. Zoletnik, "Combined hydrogen and lithium beam emission spectroscopy observation system for korea superconducting tokamak advanced research," Review of Scientific Instruments **86**, 073501 (2015).

Evolution of intermittent filaments in the scrape-off layer of NSTX

Supplementary material

M. Lampert,[1] A. Diallo,[1] and J. R. Myra[2]

[1)]*Princeton Plasma Physics Laboratory, Princeton, NJ, United States of America*[a)]

[2)]*Lodestar Research Corporation, Broomfield, CO, United States of America*

I. SCOPE

This preliminary draft manuscript provides an overview of the comparison between L and H-mode filamentary dynamics and serves as supplementary material for the publication titled "Evolution of intermittent filaments in the scrape-off layer of NSTX". This material is stored along with the data used in that publication and is presented without detailed discussion, references or data availability which is deferred to a future publication.

II. FILAMENT PARAMETERS IN L-MODE AND H-MODE REGIMES

In this supplementary material, the analyses of L-mode and H-mode discharges were separated to show the difference between these regimes to the curious reader.

There are 20 L-mode and 58 H-mode discharges in the 86 shot database. In the case of the missing 8 discharges, the confinement regime of the plasma in the analyzed time-range could not be identified neither as L- nor H-mode.

A. Parameter histograms

Figure 1 shows the estimated blob parameter's distributions for the L-mode and the H-mode plasmas in the database.

It is visible that in some cases, especially in the case of the filament angle, the distributions differ. The differences are quantified by the first four moments of the distributions and are summarized in Table I.

[a)]The author to whom correspondence may be addressed: mlampert@pppl.gov

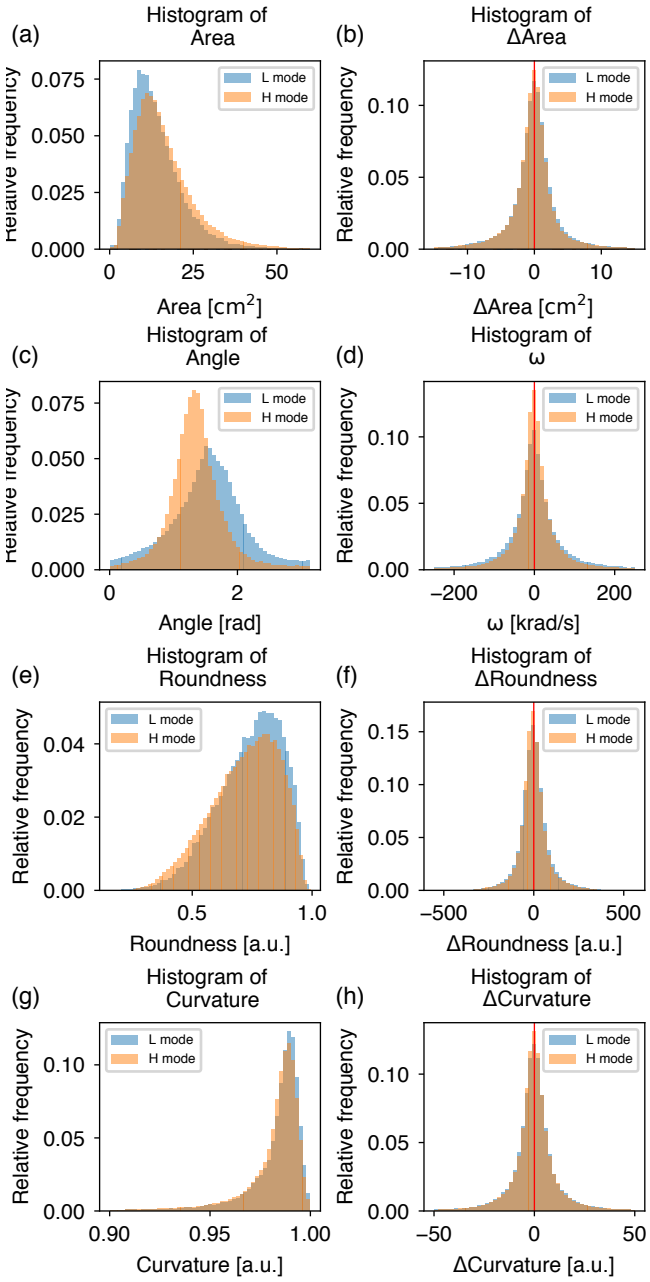

FIG. 1. Parameter histograms for the L-mode (blue) and H-mode (orange) discharges. (a), (b) area and its difference; (c), (d) angle and its time derivative; (e), (f) roundness and its time derivative; (g), (h) total curvature and its time derivative.

B. Pearson matrix

In this section, the Pearson matrices are shown separately for the L-mode and the H-mode plasmas. Figure 2 shows the Pearson correlation coefficients for L-mode plasmas.

	average		σ		skewness		kurtosis	
	L-mode	H-mode	L-mode	H-mode	L-mode	H-mode	L-mode	H-mode
Area [cm^2]	14.018	16.254	7.603	9.186	1.423	1.630	3.448	4.791
ΔArea [cm^2/sample]	-0.136	-0.231	4.201	4.377	0.024	-0.173	12.093	17.503
Angle [rad]	1.531	1.354	0.573	0.426	-0.038	0.578	0.305	2.277
ω [krad/s]	-1.446	-0.569	114.145	91.459	-0.013	0.018	8.934	14.317
Roundness [a.u.]	0.741	0.718	0.134	0.142	-0.672	-0.528	0.125	-0.331
ΔRoundness [a.u.]	1.244	-1.460	85.939	80.074	0.308	0.191	3.758	3.924
Curvature [a.u.]	0.983	0.981	0.016	0.017	-3.742	-3.696	21.985	21.924
ΔCurvature [a.u.]	-0.087	-0.126	15.858	15.087	-0.006	-0.043	22.453	27.821

TABLE I. Filament distribution moments for L-mode and H-mode plasmas

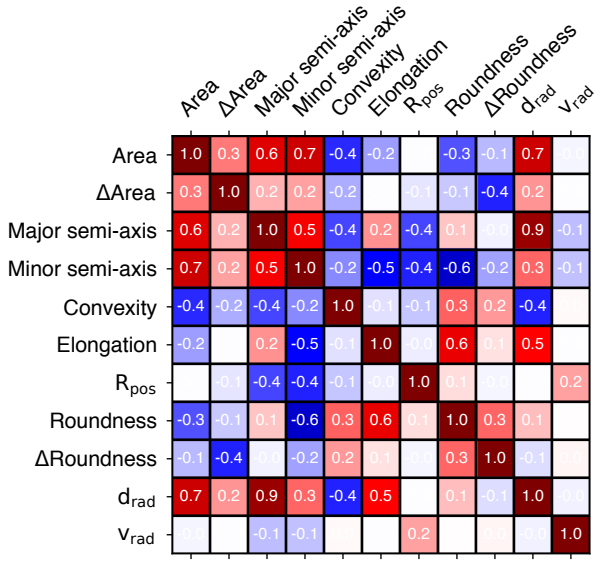

FIG. 2. Pearson correlation coefficients for L-mode plasma filament parameters.

Figure 3 presents the correlation coefficients for H-mode plasmas.

To quantify the different between the two matrices above, the difference between the H-mode and the L-mode results was calculated. The results are shown in Figure 4. A positive value shows higher correlation for H-mode plasma, while negative value shows higher correlation for L-mode

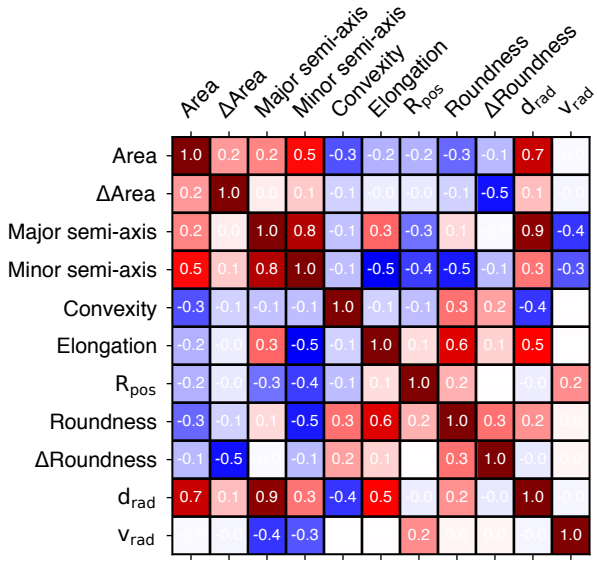

FIG. 3. Pearson correlation coefficients for H-mode plasma filament parameters.

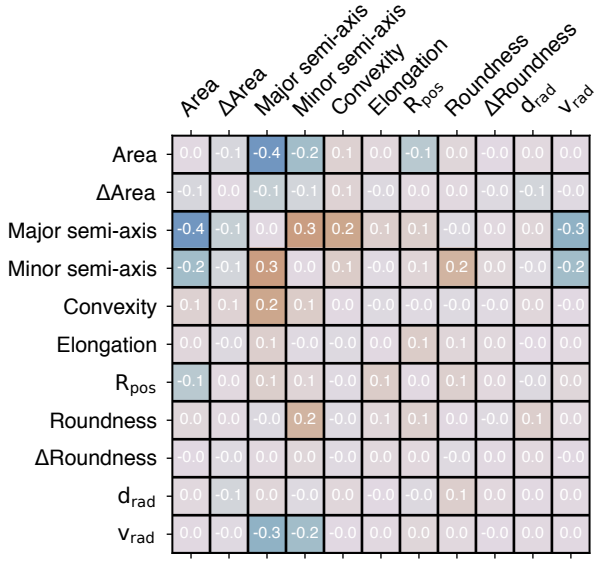

FIG. 4. Difference between the H-mode and the L-mode correlation coefficients. Positive number means the H-mode, negative number means the L-mode coefficients are higher.

plasmas.

There are slight differences visible between L and H-mode plasma blob behavior, especially between their fitted ellipse sizes and the radial velocity.

C. Two-dimensional distributions

The two-dimensional distributions were plotted each for the L-mode and for the H-mode plasma cases in Fig. 5 and Fig. 6, respectively. Similar behavior is seen between the two plasma regimes.

A quantitative assessment of the similarities can be given by calculating the numerical differences between the probability values. The result of the calculation is depicted in Fig. 7.

The largest differences are found between the convexity vs area, radial position vs radial velocity and Radial position vs major semi-axes.

D. Dependence between blob and plasma parameters

The plasma parameters characteristic to the blob observation times were compared to the blob parameters by plotting them as a function of each other. The results are plotted in Fig. 8. The L-mode results are plotted in blue while the H-mode results are shown in orange.

It is visible that there are differences between the two regimes. These are caused mainly by the different electron density and electron pressure ranges L-mode and H-mode shots have. The trends are very similar and the signs of slopes of the fitted lines remain the same for all of the trends. Further investigation of the differences are deferred to a future publication.

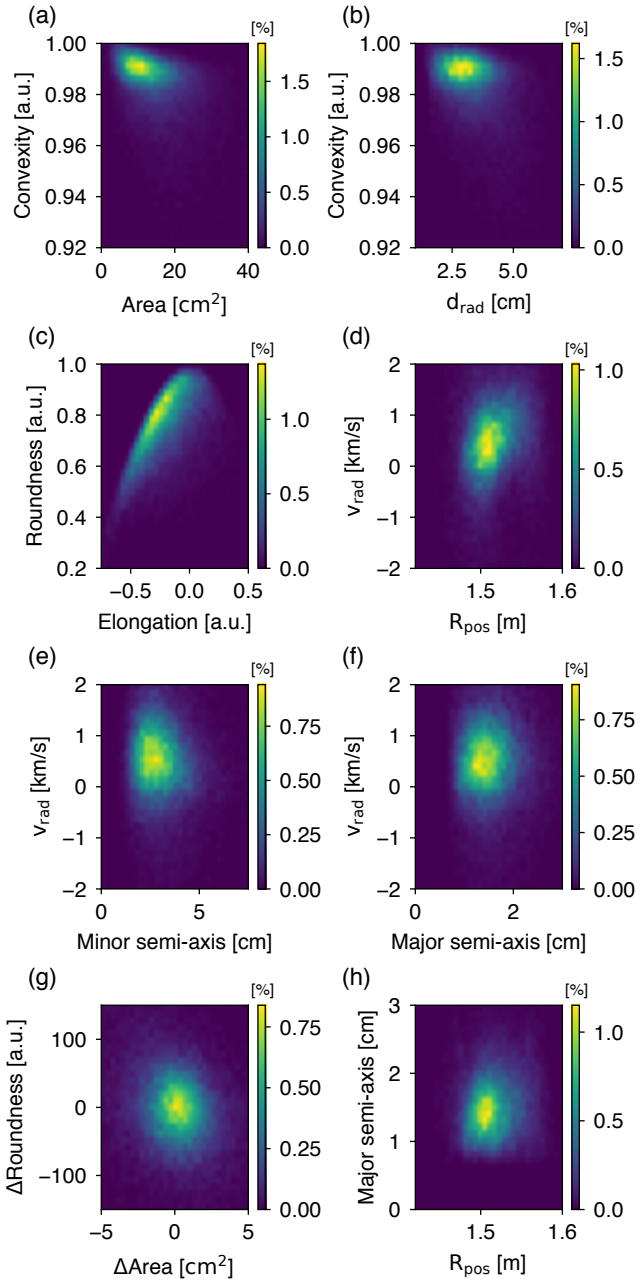

FIG. 5. Two-dimensional probability distributions of selected filament parameters for L-mode plasmas. (a) Area vs. convexity; (b) Radial size vs. convexity; (c) Elongation vs. roundness; (d) Radial position vs. radial velocity; (e) Major semi-axis vs. radial velocity; (f) Minor semi-axis vs. radial velocity; (g) Area ratio vs. roundness difference; (h) Radial position vs. major semi-axis.

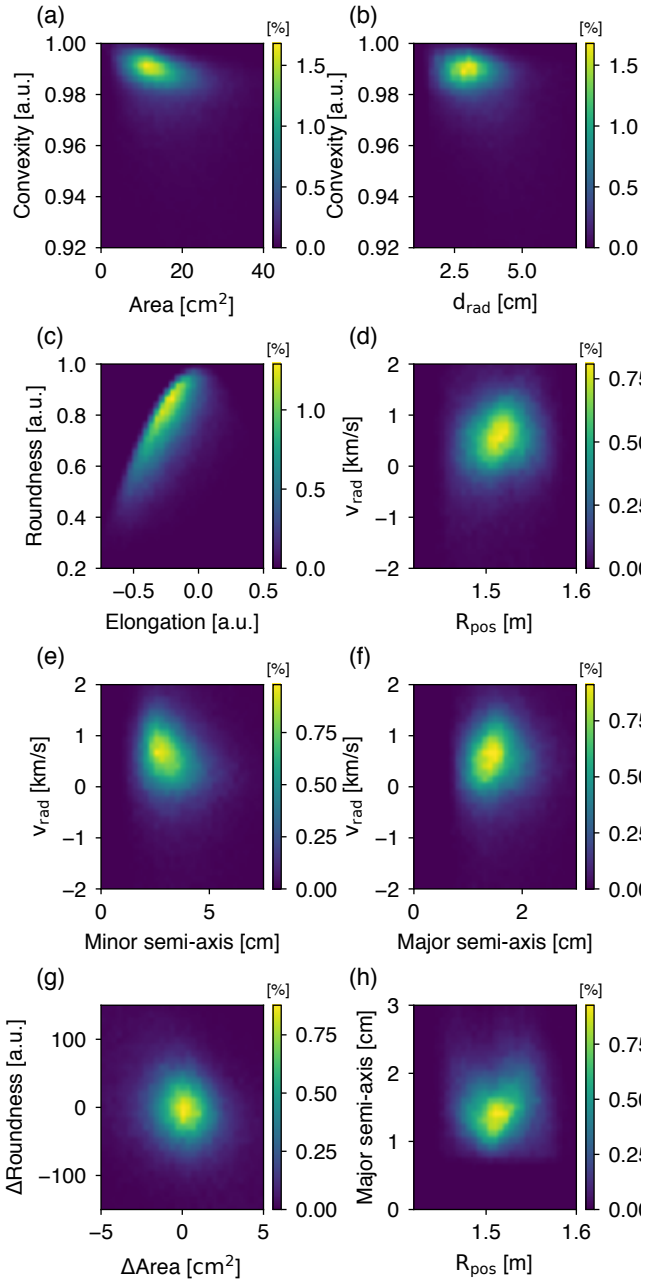

FIG. 6. Two-dimensional probability distributions of selected filament parameters for H-mode plasmas. (a) Area vs. convexity; (b) Radial size vs. convexity; (c) Elongation vs. roundness; (d) Radial position vs. radial velocity; (e) Major semi-axis vs. radial velocity; (f) Minor semi-axis vs. radial velocity; (g) Area ratio vs. roundness difference; (h) Radial position vs. major semi-axis.

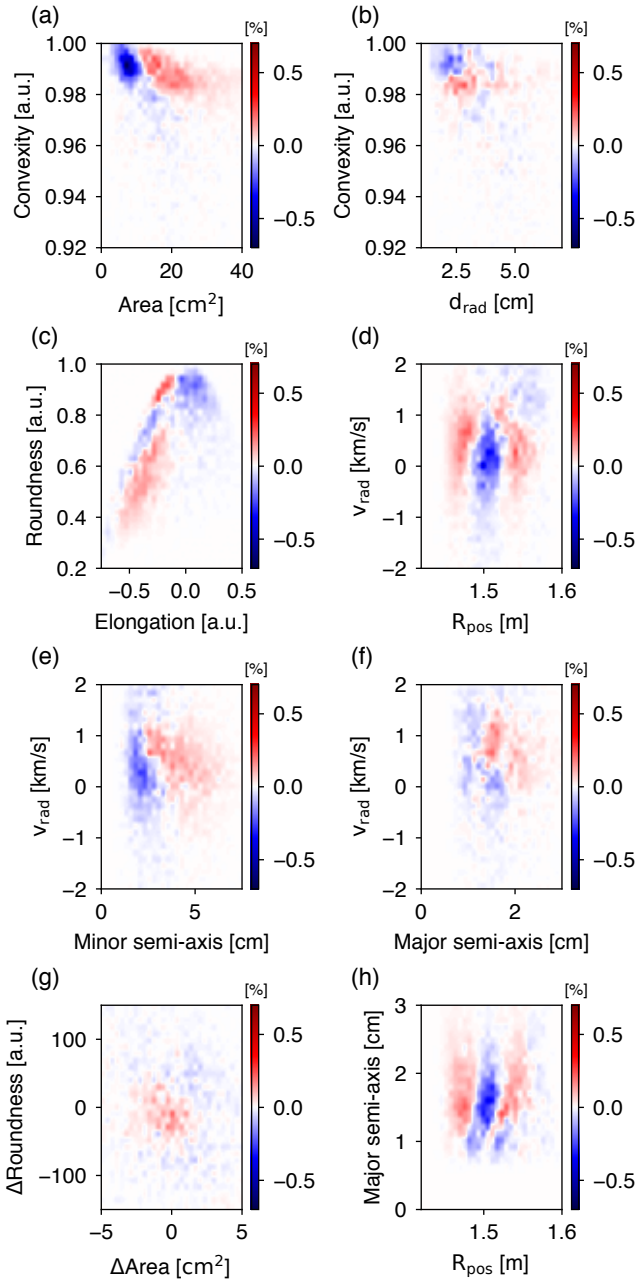

FIG. 7. Differences of the two-dimensional probability distributions between L-mode and H-mode plasmas. Positive value means the H-mode distribution has a higher probability. (a) Area vs. convexity; (b) Radial size vs. convexity; (c) Elongation vs. roundness; (d) Radial position vs. radial velocity; (e) Major semi-axis vs. radial velocity; (f) Minor semi-axis vs. radial velocity; (g) Area ratio vs. roundness difference; (h) Radial position vs. major semi-axis.

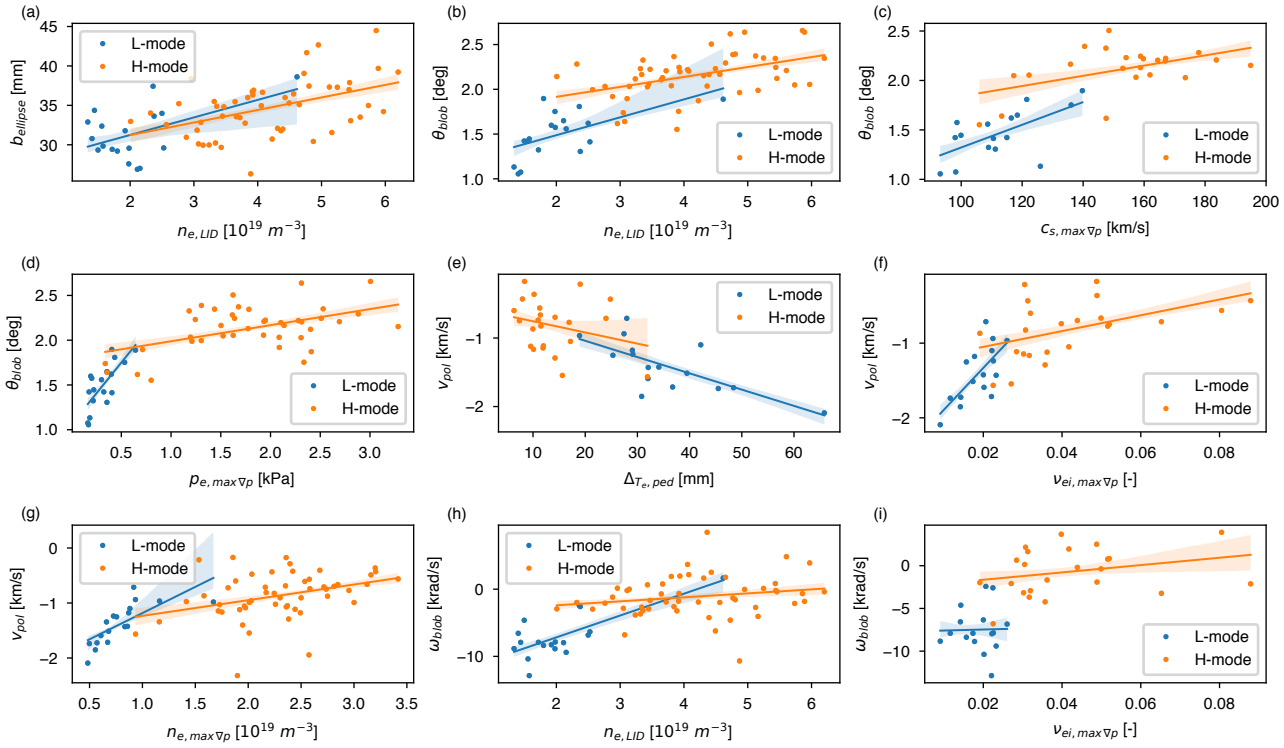

FIG. 8. Trends between selected plasma parameters during gas puff imaging (GPI) injection and the corresponding average blob parameters. Each subplot displays the Pearson correlation coefficient quantifying the linear relationship between the variables. The orange line indicates the best-fit linear regression, with the shaded region representing the 1σ confidence interval. (a) Line integrated electron density, $n_{e,LID}$, vs the minor semi-axis of the fitted ellipse, $b_{ellipse}$; (b) $n_{e,LID}$ vs the angle of the blob, θ_{blob}, with respect to horizontal; (c) the ion sound speed at the steepest electron pressure gradient, $c_{s,max\nabla p}$, vs θ_{blob}; (d) the electron pressure at the steepest electron pressure gradient, $p_{e,max\nabla p}$, vs θ_{blob}; (e) Electron temperature pedestal width, $\Delta_{T_e,ped}$, vs the poloidal velocity v_{pol}; (f) Electron-ion collisionality at the steepest electron pressure gradient, $\nu_{ei,\nabla p_{e,max}}$, vs v_{pol}; (g) The electron density at the steepest electron pressure gradient, $n_{e,\nabla p_{e,max}}$, vs v_{pol}; (h) $n_{e,LID}$ vs the angular velocity of the blobs ω_{blob}; (i) $\nu_{ei,\nabla p_{e,max}}$ vs ω_{blob}.